

MUCIG Therapy

1
2
3
4
5
6
7
8
9
10
11
12
13
14
15
16
17
18
19
20
21
22
23
24
25
26
27
28
29
30
31
32
33
34
35
36

Multiplexed repression of immunosuppressive genes as combinatorial cancer immunotherapy

Feifei Zhang^{1,2,3,*}, Guangchuan Wang^{1,2,3,*^}, Ryan Chow^{1,2,3,4,5,*},
Emily He^{1,2,3,6}, Medha Majety^{1,2,3,6}, Yueqi Zhang^{1,2,3 ^^}
and Sidi Chen^{1,2,3,4,5,7,8,9,11,@,#}

Affiliations:

1. Department of Genetics, Yale University School of Medicine, New Haven, Connecticut, USA
2. System Biology Institute, Yale University, West Haven, Connecticut, USA
3. Center for Cancer Systems Biology, Yale University, West Haven, Connecticut, USA
4. M.D.-Ph.D. Program, Yale University, West Haven, Connecticut, USA
5. Molecular Cell Biology, Genetics, and Development Program, Yale University, New Haven, CT, USA
6. Yale College, New Haven, Connecticut, USA
7. Immunobiology Program, Yale University, New Haven, Connecticut, USA
8. Yale Comprehensive Cancer Center, Yale University School of Medicine, New Haven, Connecticut, USA
9. Yale Stem Cell Center, Yale University School of Medicine, New Haven, Connecticut, USA
10. Yale Center for Biomedical Data Science, Yale University School of Medicine, New Haven, Connecticut, USA
11. Lead Contact

[^] Present Address: State Key Laboratory of Molecular Biology, Shanghai Institute of Biochemistry and Cell Biology, Center for Excellence in Molecular Cell Science, Chinese Academy of Sciences, Shanghai, China

^{^^} Present Address: Xiangya School of Medicine, Changsha, Hunan, China

* Co-first authors

@ Correspondence:

SC (sidi.chen@yale.edu)
+1-203-737-3825 (office)
+1-203-737-4952 (lab)

Lead contact.

MUCIG Therapy

37

38 **Summary**

39 A complex set of pathways maintain an immunosuppressive tumor microenvironment (TME). Current
40 cancer immunotherapies primarily rely on monoclonal antibodies targeting immune checkpoints, blocking
41 one target at a time. Here, we devise Multiplex Universal Combinatorial Immunotherapy via Gene-silencing
42 (MUCIG), as a versatile cancer immunotherapy approach. We harness CRISPR-Cas13d to efficiently target
43 multiple endogenous immunosuppressive genes on demand, allowing us to silence various combinations of
44 multiple immunosuppressive factors in the TME. Intratumoral AAV-mediated administration of MUCIG
45 (AAV-MUCIG) elicits significant anti-tumor activity with several Cas13d gRNA compositions. A
46 simplified off-the-shelf AAV-MUCIG with four gene combination (PGGC: *Pd11*, *Galectin9*, *Galectin3* and
47 *Cd47*) has anti-tumor efficacy across different tumor types and shows abscopal effect against metastatic
48 cancer. AAV-PGGC remodeled the TME by increasing CD8⁺ T cell infiltration and reducing myeloid-
49 derived immunosuppressive cells (MDSCs). Combining AAV-PGGC with Anti-Gr1 antibody that targets
50 MDSCs achieves synergistic effect against metastatic cancer, which reduces tumor burden and extends
51 survival.

52

53

MUCIG Therapy

54

55 **Introduction**

56 Cancer cells engage a variety of pathways to mold an immunosuppressive tumor microenvironment (TME)
57 that favors tumor progression and therapy resistance (Binnewies et al., 2018; Rabinovich et al., 2007;
58 Tormoen et al., 2018). This immunosuppressive TME is often initiated from the primary tumor,
59 subsequently evolving into a network of interlocking immunosuppressive mechanisms (Kim et al., 2006;
60 Munn and Bronte, 2016; Rabinovich et al., 2007). For instance, tumors hyperactivate immune checkpoints
61 to attenuate the effectiveness of T cells, allowing tumors to escape immune surveillance, suppress anti-
62 tumor immunity, and hamper effective anti-tumor immune responses (Buchbinder and Desai, 2016). By
63 targeting these key inhibitory receptors, immune checkpoint blockade (ICB) therapy can unleash anti-tumor
64 T cell responses (Pardoll, 2012; Wei et al., 2018). In particular, PD-1/PD-L1 and CTLA-4 blockade have
65 demonstrated significant clinical benefit in multiple tumor types (Sharma et al., 2021). However, many
66 patients do not respond to single agent or even combination ICB therapy. Consistent with their distinct
67 mechanisms of action, concurrent combination therapy with anti-PD-1/PD-L1 plus anti-CTLA-4 appears
68 to increase response rates above that of the corresponding monotherapies (Hammers et al., 2014; Rotte,
69 2019; Wolchok et al., 2013). These findings highlight the possibility that novel immunotherapy
70 combinations may further increase the proportion of patients who respond to ICB.

71

72 One major factor that limits the efficacy of ICB is that the immunosuppressive TME is highly dynamic and
73 unique to each patient, even for patients with the same cancer type (Sharma et al., 2017). Given the
74 complexity and heterogeneity of the TME, targeting a single gene alone is often insufficient to provide
75 clinical benefit to a broad range of patients. However, current immune checkpoint therapies primarily rely
76 on monoclonal antibodies, blocking one target at a time. Two or more antibodies have been used in
77 combination; however, the difficulties for the approach of combining more and more antibodies scale
78 exponentially, as development of each specific and potent therapeutic antibody is a daunting task by itself.
79 A more flexible, versatile, and effective means for combinatorial immunotherapy is urgently needed.

80

81 Gene silencing offers a universal approach for reducing the expression of virtually any genes in the
82 mammalian genome. Gene silencing methods include RNA interference (RNAi), CRISPR interference
83 (CRISPRi), and more recently other RNA-targeted CRISPR effectors (Boettcher and McManus, 2015;
84 Granados-Riveron and Aquino-Jarquín, 2018). Simultaneous silencing of multiple genes has been readily
85 achievable by multiplexing of target-specific guide sequences, such as short-hairpin RNAs (shRNAs), or
86 CRISPR guide RNAs (gRNAs), as all genes' silencing use the same mechanism and the same backbone

MUCIG Therapy

87 machinery with these methods. Therefore, we reasoned that gene silencing may provide unique benefit for
88 a substantially simpler, and more versatile approach for multiplexing targeting of immune genes. With the
89 versatility of gene silencing, we further hypothesized that targeting multiple immunosuppressive genes in
90 the TME would elicit anti-tumor immunity.

91

92 Here, we developed Multiplex Universal Combinatorial Immunotherapy via Gene-silencing (MUCIG), as
93 a versatile cancer immunotherapy approach. The recently discovered CRISPR/Cas13 systems have been
94 demonstrated as efficient tools for RNA knockdown, as Cas13 proteins can bind and cleave endogenous
95 RNAs in a programmable manner through the use of sequence-specific gRNAs (Granados-Riveron and
96 Aquino-Jarquin, 2018). RfxCas13d (also known as CasRx) was reported as one such RNA targeting tool
97 (Koneremann et al., 2018; Yan et al., 2018), with a compact size of 990 amino acids that is considerably
98 smaller than Cas13a-c effectors or Cas9, making it feasible to package both gRNAs and Cas13d into a
99 single Adeno-associated virus (AAV) construct (Koneremann et al., 2018). Moreover, Cas13d is
100 immunogenic, the antigen of which could induce T cell proliferative responses and increase CD4+T cell
101 secreting IFN- γ or TNF- α (Tang et al., 2022), which could be utilized to enhance the tumor immune
102 response. Harnessing CRISPR/Cas13d-based RNA targeting system for MUCIG, we set out to test the
103 concept of combinatorial immunotherapy by simultaneously knocking down multiple immunosuppressive
104 genes in the TME *in vivo*.

105

106

107 **Results**

108 **Efficient knockdown of endogenous immune suppressive genes using Cas13d**

109 To assess the efficiency of Cas13d-mediated RNA knockdown, we first established a Hepa1-6 tumor cell
110 line stably expressing Cas13d-GFP. We transfected gRNAs into the cells, and performed flow cytometry
111 analysis of gene expression 2 days after transfection (**Figure S1A**). To identify effective gRNAs for
112 Cas13d-mediated knockdown efficiency of *Pd11* (*Cd274*), we screened 40 Cas13 gRNAs that targeted the
113 *Pd11* mRNA sequence (**Figure S1B**). Flow cytometry analysis showed that 29 out of 40 gRNAs could
114 successfully knock down PDL1 protein (**Figure S1C**). Among all the gRNAs, g14 showed the best
115 knockdown efficiency, resulting in $56\% \pm 0.079\%$ reduction of PDL1. Similarly, we designed 25 gRNAs
116 targeting *Galectin9* (*Lgals9*) and assessed knockdown efficiency. We found that transfection of g9 could
117 successfully knock down GALECTIN9 by $45\% \pm 0.073\%$ (**Figure S1D**).

118

MUCIG Therapy

119 A computational model to predict Cas13d gRNAs was recently developed (Wessels et al., 2020). To further
120 improve the Cas13d gRNA design for immune genes, we applied this design tool to design 4 to 5 gRNAs
121 for 4 different immunosuppressive genes of interest: *Cd47*, *Galectin3 (Lgals3)*, *Cd66a*, and *Cd200*. To
122 assess the efficiency of these tool-designed gRNAs, we generated an all-in-one vector including gRNA,
123 Cas13d and selection marker EGFP (**Figure S2A**). We performed flow cytometry to gate the GFP positive
124 cells, and then analyzed gRNA knockdown efficacy by fluorescent intensity. We found that the designed
125 gRNAs could efficiently knock down the target genes (**Figure S2B**). For all 4 targeted genes, we identified
126 at least one gRNA for each target gene that achieved over 50% knockdown efficiency. For *Cd66a*, all 5
127 designed gRNAs showed robust knockdown. These data indicated that the Cas13d gRNA design tool is
128 predictive and reliable for the following multiplex genes targeting. To achieve stronger gene repression, we
129 compared the knockdown efficiency of gRNAs bearing the wildtype direct repeat (WT-DR) vs. a mutant
130 DR (Mut-DR), which was previously described to have improved efficiency (Wessels et al., 2020). The
131 WT-DR or the Mut-DR-gRNA plasmid was transfected into E0771-Cas13d overexpressing cells (**Figure**
132 **S2C**). The knockdown of PDL1 is less efficient in E0771 cells with the WT-DR g14 (~11%) (**Figure S2D**).
133 In contrast, the Mut-DR g14 could achieve ~68% PDL1 knockdown at protein level. Flow cytometry
134 analysis showed that using a mutated DR with the PDL1 gRNA improved the knockdown efficacy by $57\% \pm 0.026\%$
135 $\pm 0.026\%$ when compared to WT-DR (**Figure S2D**). For *Cd73* gRNA, we similarly observed $26.4 \pm 0.031\%$
136 improvement with Mut-DR. We also compared the knockdown efficacy between Cas13d-mediated gRNAs
137 and shRNAs, illustrating that Cas13d-mediated gRNA had better or similar knockdown than shRNAs, for
138 the same genes in the same cell types, even if we used the WT-DR (**Figure S2E&F**). These data indicate
139 that Cas13d-gRNA-mediated knockdown is an effective approach to repress the expression of tumor
140 intrinsic immune suppressive genes.

141

142 Recently, Cas13d was reported to have collateral activity in human cells (Kelley et al., 2021; Shi et al.,
143 2021; Wei et al., 2022). It was reported that when targeting the transfected DsRed in HEK cells, the co-
144 transfected reporter gene GFP would be markedly down-regulated (Shi et al., 2021). However, when
145 targeting the endogenous RNAs, the extent of collateral activity could be influenced by the abundance of
146 the target RNA. To test how strong the collateral activity when targeting the endogenous
147 immunosuppressive genes, we generated a GFP and mCherry dual reporter system to indicate the collateral
148 activity of Cas13d (**Figure S3A**). Instead of transient transfection of the reporter gene plasmids, we
149 established an E0771 cell line stably expressing Cas13d, GFP and mCherry protein by lentivirus
150 transduction to better mimic the endogenous gene expression. According to the flow cytometry results, both
151 the GFP and mCherry reporters showed stable expression among all the tested guide RNAs targeting the

MUCIG Therapy

152 immunosuppressive genes, including non-transduced control (NTC) and empty vector (EV) (**Figure S3B**).
153 Furthermore, we tested the specific gene targeting of these guide RNAs at protein by flow cytometry
154 (**Figure S3B**). Even though scramble control caused a very mild background knockdown of PDL1 or
155 GALECTIN9, the on-target knockdown is still much stronger (**Figure S2B**). Then RT-qPCR was performed
156 to test the gene knockdown at RNA level. The data and statistical test among groups showed specific
157 targeting of all the guide RNAs (**Figure S3C**). These data suggested specific on-target of the Cas13d guide
158 RNAs when targeting the endogenous immunosuppressive genes.

159

160 **AAV-mediated immunosuppressive gene repression as an immunotherapeutic modality**

161 Given that gene knockdown is not complete by Cas13d, the natural question is whether such degree of
162 knockdown can lead to effective immune modulation, and thereby anti-tumor immunity *in vivo*. AAV is
163 one of the leading vehicles for transgene delivery (Wang et al., 2019a). To evaluate the feasibility of *in vivo*
164 Cas13d and gRNA intratumoral delivery, we first generated an AAV vector expressing firefly luciferase
165 and GFP (AAV-Luci-GFP). We intratumorally injected AAV-Luci-GFP into E0771 tumor-bearing mice
166 and analyzed luciferase activity by *in vivo* bioluminescent imaging (**Figure S4**). The time course imaging
167 showed that luciferase was persistently expressed primarily in the tumor and, unsurprisingly, also in the
168 liver (**Figure S4**). These data indicate that intratumoral AAV injection can successfully deliver genetic
169 cargo into tumor.

170

171 Having evaluated the feasibility of the Cas13d gRNA knockdown system, we next sought to investigate
172 whether silencing multiple immunosuppressive genes in the TME via AAV delivery of Cas13d and gRNAs
173 could function as a combinatorial immunotherapy. We termed this approach MUCIG (Multiplex Universal
174 Combinatorial Immunotherapy via Gene-silencing). We first designed different scales of gene library pools
175 targeting combinations of immunosuppressive genes (**Figure 1A, B**). Our first gene library pool was
176 designed on the basis of several criteria. By leveraging the knowledge from the literature and the
177 immunogenomic databases such as TISIDB (Ru et al., 2019), we identified 588 tumor immunosuppressive
178 genes and 535 tumor immunostimulatory genes (**Figure 1B**). In order to avoid undesired side effects, we
179 excluded these tumor immunostimulatory genes. We also excluded tumor suppressor genes (TSGs) to avoid
180 potential pro-tumor effect by TSG knockdown, and excluded house-keeping genes to avoid potential
181 toxicity associated with killing normal cells by essential gene knockdown (**Figure 1B**). We further
182 considered the top hits identified from functional screens for genetic factors that enable cancer cells to
183 escape the immune system (Ishizuka et al., 2019; Manguso et al., 2017; Shen et al., 2004; Wang et al.,
184 2021), selecting genes that have been experimentally validated to be cancer immunotherapy targets. Next,

MUCIG Therapy

185 we identified a core set of genes which were recently identified as cancer-intrinsic T cell killing evasion
186 genes across at least 3 cancer models (Lawson et al., 2020). Thus, we curated a total of 125 genes from
187 screen data. With a tiered approach, we designed four initial Cas13d gRNA pools for MUCIG experiments
188 (MUCIG-pool1: 313 genes, pool2: 152 genes; pool3: 55 genes; pool4, 19 genes) (**Figure 1B**). We designed
189 Cas13d gRNA pools targeting these gene pools, with 5 gRNAs per gene for most genes.

190
191 To facilitate direct delivery of these pools into tumors, we generated an all-in-one AAV vector (AAV-U6-
192 gRNAs-EFS-Cas13d) (**Figure 1A**), which includes both Cas13d and guide-RNA. We synthesized and
193 cloned the gRNA pools and produced the four AAV-MUCIG viral pools accordingly. To evaluate the *in*
194 *vivo* efficacy of these gene pools against tumors, we first utilized a syngeneic orthotopic tumor model of
195 triple negative breast cancer (TNBC) (E0771 in C57BL/6 mice), which is known to be moderately
196 responsive to immunotherapy. C57BL/6Nr (B6) mice bearing E0771 fat pad transplanted tumors were
197 treated with AAV-MUCIG pools by intratumoral viral administration. All AAV-MUCIG-pools treatment
198 led to significantly reduced tumor burden compared to the AAV-vector or PBS treatment (**Figure 1C**).
199 Among the 4 gene pools, MUCIG-pool4 showed significantly better, and pool2 showed moderately better,
200 therapeutic effect than pool1 and pool3, with AAV-MUCIG-pool4 showing the strongest efficacy among
201 the four (**Figure 1C&D**). These data indicated that all four compositions of AAV-MUCIG treatment had
202 therapeutic effect in this tumor model. Different scale and composition of gene pools showed different
203 extent tumor burden reduction effect, which could be influenced by the composition of the genes, the
204 relative concentration of each gRNA, the effects of silencing, and other combinatorial effects.

205

206 **A four-gene AAV-MUCIG composition elicits potent anti-tumor immunity**

207 While two of the AAV-MUCIG gene pools had evidence of anti-tumor responses, we reasoned that further
208 optimization of the library might increase treatment efficacy by reducing the proportion of potential neutral
209 or detrimental gRNAs that are delivered to the tumor. To further refine the MUCIG-pool4, we assessed
210 protein-level expression of the genes targeted in MUCIG-pool4 across a panel of syngeneic cancer cell lines
211 that represent various tumor types. As we were primarily interested in assessing tumor-derived factors, we
212 excluded the genes that are primarily expressed in non-tumor cells, such as the T cell checkpoints *Pdcd1*,
213 *Lag3*, and *Havcr2/Tim3*, acknowledging that these genes are also immunosuppressive genes that could
214 potentially be effectively targeted via other approaches. In addition to the genes targeted in pool4, we also
215 tested other known immunosuppressive genes, such as *Tgf- β* . We systematically analyzed 17 genes by flow
216 cytometry, both for surface and intracellular expression, in ten different syngeneic cell lines across nine
217 different cancer types (MB49 bladder cancer, MC38 colon cancer, Hepa liver cancer, GL261 brain cancer,

MUCIG Therapy

218 Pan02 pancreatic cancer, A20 lymphoma, Colon 26 colon cancer, E0771 breast cancer, B16F10 melanoma,
219 and LLC lung cancer lines) (**Figure 2A&B**). Through this unbiased combined immune gene expression
220 analysis, we pinpointed 4 genes (*Pd11/Cd247*, *Cd47*, *Galectin9/Lgals9*, and *Galectin3/Lgals3*) that were
221 abundantly expressed at the protein-level across different cancer cell types (**Figure 2A-D**). We also
222 examined the human cancer gene expression database and confirmed that the human orthologs of these
223 genes are expressed across a variety of human tumors, supporting their clinical relevance (Tang et al., 2019).

224

225 From the flow data, GALECTIN9 and GALECTIN3 were exclusively expressed intracellularly among all
226 cell lines (**Figure 2C&D**). Of note, current standard monoclonal antibodies can not inhibit such intracellular
227 targets, however this is achievable by Cas13d-mediated silencing as we showed above (**Figure S3**). CD47
228 was highly expressed on the surface and also expressed intracellularly (**Figure 2C&D**). Surprisingly, PDL1
229 was highly expressed intracellularly, even in cell lines with absent surface expression of PDL1 (**Figure**
230 **2C&D**). Since immune checkpoints are often induced in the process of tumorigenesis, we tested expression
231 of these genes in an *in vivo* E0771 tumor model, by flow cytometry analysis of these four proteins in
232 dissociated single cells from tumor samples. Our results showed that all four factors (PDL1, CD47,
233 GALECTIN9 and GALECTIN3) were expressed in both tumor and immune cells (**Figure 2E**).

234

235 We then designed a gRNA composition targeting these four genes as a rational and simplified version of
236 MUCIG (named **PGGC** for *Pd11;Galectin9;Galectin3;and Cd47*), with one of the top gRNA for each gene.
237 We then delivered the AAV-PGGC pool into E0771 tumor-bearing mice by intratumoral injection (**Figure**
238 **2F**). We found that treatment with AAV-PGGC (*Pd11-g14*, *Galectin9-g9*, *Galectin3-g2*, *Cd47-g2*) led to
239 significant reduction of tumor growth, with an efficacy level similar to the AAV-pool4 group despite that
240 PGGC only targets 4/19 genes chosen from pool4. (**Figure 2G&H**). To assess whether these effects were
241 more broadly applicable to other tumor models, we similarly evaluated the anti-tumor effect of AAV-PGGC
242 in three representative models with different levels of responsiveness to immune checkpoint blockade
243 antibody therapeutics, including B16F10 melanoma (resistant) (**Figure 3A&B**), Colon26 colon cancer
244 (sensitive) (**Figure 3C&D**), and Pan02 pancreatic cancer (resistant) (**Figure 3E&F**) mouse models. In all
245 three models, AAV-PGGC showed significant *in vivo* anti-tumor efficacy when compared with the control
246 group (**Figure 3A-F**). Importantly, in these three models where AAV-pool4 treatment failed to reduce
247 tumor growth, AAV-PGGC still demonstrated significant efficacy across all models (**Figure 3**). These data
248 suggest that this four gene formula of Cas13d/gRNA-pool (AAV-PGGC) is effective across different cancer
249 types in animal models.

250

MUCIG Therapy

251 **AAV-PGGC treatment promotes T cell tumor infiltration while hampering the recruitment of** 252 **immunosuppressive cells**

253 We then sought to examine how AAV-PGGC treatment influence the immune composition of the TME.
254 By flow cytometry analysis, we profiled tumor-infiltrating lymphoid and myeloid cell populations in mice
255 that received either PBS, AAV-vector, or AAV-PGGC treatment in two different syngeneic tumor models
256 (E0771 and Colon26) (**Figure 4A, S5A**). In the E0771 tumor model, we observed significantly more CD45⁺
257 tumor infiltrating immune cells in the AAV-PGGC treated mice than the Vector control group (**Figure 4B**).
258 Among the tumor infiltrating lymphocytes (TILs), we also found a significant increase of CD8⁺ and CD4⁺
259 T cells in the AAV-PGGC treated mice compared to Cas13d-vector control (**Figure 4B**). In addition, though
260 there were no substantial changes in the macrophage or the DC population, between AAV-PGGC and
261 Vector control, there was a significant decrease of MDSCs, a heterogeneous cell population with the
262 capacity to functionally suppress T cell responses (**Figure 4B**). In an independent tumor model, Colon26,
263 we similarly observed a significant increase of significantly more CD8⁺ TILs (but not CD4⁺ TILs) in the
264 AAV-PGGC treatment group compared to Vector control group (**Figure 4B**). For the innate populations in
265 the Colon26 model, in AAV-PGGC treated tumors compared to Vector control, there were more tumor-
266 infiltrating macrophages and DCs, relevant to antigen presentation and for priming adaptive immune
267 responses (**Figure 4B**). In AAV-PGGC treated tumors compared to PBS control, again there was a
268 significant decrease of MDSCs (**Figure 4B**).

269
270 To systematically investigate the effect of AAV-PGGC treatment on the immune cell populations and their
271 transcriptomics in the TME, we performed single-cell RNA-seq (scRNA-seq) of tumor-infiltrating immune
272 cells in mice treated with PBS, AAV-Vector, or AAV-PGGC (**Figure 4C&D**). Consistent with the flow
273 cytometry analysis, scRNA-seq of the E0771 tumor model revealed significant changes in multiple immune
274 cell populations after AAV-PGGC treatment (**Figure 4E**), including an increase of CD8⁺ T cells and
275 proliferating CD8⁺ T cells. Similarly, in the Colon26 model, we observed more CD8⁺ T cells and
276 proliferating CD8⁺ T cells with AAV-PGGC treatment (**Figure 4F-H**). On the other hand, there was a
277 substantial reduction of neutrophil abundances in AAV-PGGC treatment group compared with PBS or
278 vector control group (**Figure 4E**), which was also observed in the Colon26 model (**Figure 4H**).

279
280 Via differential expression analysis (DE) of sc-RNA-seq data, we identified DE genes in the cell types
281 whose abundances were most affected by AAV-PGGC, including CD8⁺ T cells, neutrophils and
282 macrophages. We found a panel of genes associated with key immunosuppressive functions were
283 downregulated across both E0771 and Colon26 models, including *Arg2*, *Il1b*, *Trem1*, *S100a8*, *S100a9*, *Tigit*,

MUCIG Therapy

284 and *Cd37* (**Figure S5B-D**). It was reported that CD37 could inhibit Cd3-induced T cell proliferation (van
285 Spruiel et al., 2004). In CD8⁺ T cells, we found *Cd37* was downregulated in AAV-PGGC treatment group
286 when compared with vector group (**Figure S5B**). *Tigit*, a marker of T cell exhaustion (Kong et al., 2016),
287 was also decreased in CD8⁺ T cells of AAV-PGGC treatment group (**Figure S5B**). *Arg2*, which has been
288 implicated in the immunosuppressive functions of neutrophils, was downregulated in the AAV-PGGC
289 group along with *Ifitm1* and *Ifitm3*, two genes that play a role in suppressing interferon mediated immunity
290 (Gómez-Herranz et al., 2019; Grzywa et al., 2020) (**Figure S5C**). *S100a8* and *S100a9*, two factors that help
291 recruit MDSCs to the TME (Srikrishna, 2012), were downregulated in macrophages and CD8⁺ T cells from
292 AAV-PGGC treated tumors (**Figure S5D**). Consistent with the observed reductions in tumor-associated
293 neutrophils after AAV-PGGC treatment, the genes encoding neutrophil-recruiting chemokines *Cxcl1* and
294 *Cxcl2* were significantly downregulated in both neutrophils and macrophages isolated from tumors treated
295 with AAV-PGGC. These data suggested that AAV-PGGC treatment can effectively reverse the
296 immunosuppressive TME, promoting T cell infiltration and reducing suppressive myeloid cell populations.

297

298 **AAV-PGGC combined with anti-GR1 treatments inhibit tumor growth and metastasis**

299 Given the increase of CD8⁺ T cells and reduction of neutrophils in the TME after AAV-PGGC treatment,
300 we next tested how these two cell populations influence the therapeutic efficacy of AAV-PGGC. We
301 performed CD8⁺ T cell or MDSC/neutrophils depletion by *in vivo* injection of anti-CD8 or anti-GR1
302 antibody, respectively (**Figure 5A**). We observed that mice with CD8⁺ T cell depletion partially impaired
303 the anti-tumor effect of AAV-PGGC (**Figure 5B&C**), which indicate that AAV-PGGC treatment is
304 partially dependent on CD8⁺ T cells. Meanwhile, depletion of MDSCs and neutrophils by anti-GR1 in
305 combination with AAV-PGGC treatment could further reduce the tumor burden when comparing to either
306 AAV-PGGC or anti-GR1 antibody alone (**Figure 5B and 5D**). These data suggested that CD8⁺ T cells and
307 MDSCs/neutrophils together play critical roles in AAV-PGGC therapy, and combinatorial treatment with
308 AAV-PGGC plus anti-GR1 have a synergistic effect.

309

310 We next sought to determine whether the local AAV-PGGC treatment induced anti-tumor effect could
311 extend to distant tumor site. We utilized a dual-sites E0771 tumor model similar to previous work (Wang
312 et al., 2019b), to evaluate the systemic anti-tumor effect of AAV-PGGC against both the injected and non-
313 injected distant sites (**Figure 6A**). In this E0771 dual tumor model, different numbers of cells were injected
314 into both mammary fat pads to model a primary tumor and a distant tumor. Then AAV-PGGC was injected
315 only to the primary tumor site. We found that AAV-PGGC inhibited tumor growth not only at the injected

MUCIG Therapy

316 primary site but also the non-injected distant site (**Figure 6B&C**). These data suggest that AAV-PGGC has
317 a systemic anti-tumor activity.

318

319 We wondered whether AAV-PGGC could have a therapeutic effect on metastatic cancer in internal organs.
320 We utilized a tumor model by fat pad injecting of E0771 cell to develop the orthotopic tumor burden, and
321 intravenous injection of luciferase-expressing E0771 to model lung metastatic tumor burden (**Figure S6A**).
322 Tumor-bearing mice were treated with AAV-PGGC by intratumoral injection, primary tumor volume was
323 measured for primary tumor burden, and bioluminescent signal was measured for lung metastatic burden.
324 Mice treated with AAV-PGGC had significant reduction of primary tumor growth (**Figure S6B**).
325 Importantly, AAV-PGGC also significantly extended lung metastasis free survival when comparing to
326 Cas13d-vector control group, with a numerical effect on overall survival (**Figure S6C-E**). These data
327 indicate AAV-PGGC local treatment has certain moderate therapeutic effect on metastatic cancer in internal
328 organs.

329

330 Because AAV-PGGC in combination with anti-GR1 antibody had synergistic anti-tumor activity, we
331 wondered whether the combined treatment could have stronger efficacy against metastases. We again
332 utilized the orthotopic inject of primary tumor and intravenous injection to model lung metastasis (**Figure**
333 **6D**). Due to the limited effect on lung metastatic tumor by local AAV-PGGC injection alone, we injected
334 AAV-PGGC by both intratumoral and intravenous injection for the goal of better metastatic tumor targeting,
335 and combined with anti-GR1+ antibody treatment given by intraperitoneal (i.p.) injection (**Figure 6D**).
336 While anti-GR1 alone has little effect, we observed significant tumor suppression by AAV-PGGC alone or
337 AAV-PGGC plus anti-GR1 combo treatment (**Figure 6E**). In this E0771 metastatic tumor model, the AAV-
338 PGGC plus anti-GR1 combo showed the strongest therapeutic effect among all treatment groups, against
339 both primary tumor and metastatic disease (**Figure 6E-H**). The effect of treatments on metastatic disease
340 were reflected by IVIS imaging of metastatic tumor burden (**Figure 6F**), metastasis-free survival (**Figure**
341 **6G**), and overall survival (**Figure 6H**). These data indicated that AAV-PGGC in combination with anti-
342 GR1 antibody treatment had significant efficacy against a systemic disease with internal organ metastasis
343 in a syngeneic orthotopic tumor model.

344

345

346 Discussion

347 The TME is enriched with immunosuppressive factors that can be derived from tumor cells, tumor-
348 associated fibroblasts or the infiltrating immunosuppressive cells (Baghban et al., 2020; Motz and Coukos,

MUCIG Therapy

349 2013; Ribeiro Franco et al., 2020). Immunosuppressive factors produced by immunosuppressive cells can
350 either inhibit effective anti-tumor immunity by their immune checkpoint function, or attract and recruit
351 immature immune cells and induce their differentiation into immune suppressive cells, such as MDSCs,
352 M2 macrophages, or regulatory T cells (Tregs) (Chang et al., 2016; Gabrilovich and Nagaraj, 2009; Hao et
353 al., 2012). They can also influence T cell access to the tumor core or inhibit T cell activation and
354 proliferation (Jiang et al., 2015). Tumor immunosuppressive factors are promising targets for therapeutic
355 intervention, as they enable tumor cells to escape elimination by the immune system. A number of
356 preclinical studies have demonstrated that neutralization of immunosuppressive factors can reverse the
357 immunosuppressive TME and promote anti-tumor immunity (Biswas et al., 2007; Ni et al., 2020).

358

359 Various strategies have been developed to repress such targets or their activity, including siRNAs, antisense
360 oligos, antagonistic antibodies, and small molecule inhibitors. However, the efficacy of monotherapies
361 targeting immunosuppressive factors is limited to only a subset of patients, prompting our efforts to explore
362 efficient approaches for combinatorial immunotherapy. Prior studies have demonstrated that cancer gene
363 therapy, such as local tumor overexpression of OX40L or other combinatorial cytokines, has the potential
364 to promote tumor regression (Haabeth et al., 2019). However, because the payloads for transgene
365 overexpression are often sizable, it will be difficult to multiplex a large number of transgenes expressing
366 immunostimulatory factors as a combinatorial therapy. Here we take the converse approach by
367 simultaneously repressing multiple immunosuppressive genes directly in the TME. We leverage the
368 modularity of the CRISPR/Cas13d system to devise multiple combinatorial immunotherapies,
369 demonstrating the anti-tumor efficacy of several different libraries of varying complexity. Because
370 multiplexing gRNAs is simple, it is readily feasible to generate and pool gRNA libraries that target a large
371 number of immunosuppressive genes.

372

373 Because the relative abundance of each gRNA will influence its silencing efficiency, as well as the
374 challenges in manufacturing, optimizing the size of the library is crucial for MUCIG therapy. We thus
375 rationally refined the library composition and tested five different compositions of libraries at different
376 scales. We demonstrate that a simple AAV-PGGC combination therapy against four immune checkpoints,
377 PDL1, CD47, GALECTIN3, and GALECTIN9, had significant anti-tumor activity in several different
378 tumor models, including breast cancer (E0771), melanoma (B16F10), pancreatic cancer (Pan02), and colon
379 cancer (Colon26). These results suggest that the concept of MUCIG is not limited to a single tumor type
380 and can potentially be broadly applicable. To understand the mechanisms of action behind the anti-tumor
381 efficacy, we investigated the TME change upon AAV-PGGC treatment by flow cytometry and scRNA-seq.

MUCIG Therapy

382 We found that AAV-PGGC therapy enhanced CD8⁺ T cell infiltration and reduced the abundances of
383 suppressive myeloid cells. On the transcriptional level, we observed consistent down-regulation of multiple
384 immunosuppressive genes in two different cancer models, and a concordant reduction in the neutrophil
385 chemoattractants CXCL1 and CXCL2. Our results showed that AAV-PGGC therapy can attenuate the
386 immunosuppressive TME, thereby enhancing anti-tumor immune responses.

387

388 Key challenges with tumor gene therapy include on-target-specificity and gene delivery efficiency. Cas13d
389 binds and cleaves single-strand RNA, thus avoiding safety concerns stemming from unintended DNA
390 damage caused by Cas9 or Cas12a. In addition, Cas13d is more compact compared to Cas9, Cas12a, and
391 many other Cas13 family members, conferring a key advantage for viral vector delivery (Konermann et al.,
392 2018). We utilized AAVs to deliver the Cas13d-gRNA payload into tumors, as AAVs can efficiently deliver
393 foreign genetic materials *in vivo* with minimal toxicity. Indeed, we observed persistent exogenous gene
394 expression up to two weeks after the final intratumoral injection of AAV. However, as we observed here,
395 one potential safety limitation of intratumoral AAV delivery is the propensity for AAVs to transduce cells
396 in the liver, although we did not observe obvious gross side effects in any of the MUCIG-treated mice.
397 AAV-mediated delivery still poses safety concerns relative to non-viral approaches, as the AAV genome
398 can integrate into the host cell genome and double-strand break sites (Deyle and Russell, 2009). In addition,
399 the diversity of immunosuppressive pathways that are engaged across different tumors poses an important
400 challenge. Nevertheless, the MUCIG approach, with the versatility of targeting virtually any reasonable
401 combinations of genes using CRISPR-Cas13d and gRNA pools, offers far greater flexibility and modularity
402 compared to conventional antagonistic antibodies or small molecules. By further customizing the cocktail
403 of immunosuppressive factors that is targeted by MUCIG, or by utilizing more specific delivery vehicles,
404 we anticipate that the therapeutic window can be optimized to minimize off-tumor toxicity while
405 maintaining anti-tumor efficacy.

406

407 In summary, here we present a proof-of-principle demonstration of MUCIG, a versatile strategy for
408 combinatorial cancer immunotherapy by multiplexed targeting of the immunosuppressive gene collections.
409 By simultaneously unraveling multiple facets of the immunosuppressive TME, MUCIG is able to drive
410 customized anti-tumor immunity and thereby therapeutic efficacy against both primary tumor and distant
411 metastatic disease. MUCIG can in principle be rapidly customized for targeting any combinations of
412 immunosuppressive genes in diverse cancer types.

MUCIG Therapy

413

414 **Author Contributions**

415 Conceptualization: SC. Design: RZ, GW, RC, SC. Experiment lead: FZ, GW. Analytic lead: RC.
416 Experiment assistance and support: EH, MM, YZ. Manuscript prep: FZ, RC, GW, SC. Supervision and
417 funding: SC.

418

419 **Acknowledgments**

420 **Institutional approval**

421 This study has received institutional regulatory approval. All recombinant DNA and biosafety work was
422 performed under the guidelines of Yale Environment, Health and Safety (EHS) Committee with an
423 approved protocol (Chen-rDNA-15-45). All animal work was approved by Yale University's Institutional
424 Animal Care and Use Committee (IACUC) and performed with approved protocols (Chen #2018-20068;
425 #2021-20068).

426

427 **Discussion and Support**

428 We thank all members in Chen laboratory, as well as various colleagues in Yale Genetics, SBI, CSBC,
429 MCGD, Immunobiology, BBS, YCC, YSCC, and CBDS for assistance and/or discussions. We thank
430 various Yale Core Facilities such as YCGA, HPC, WCAC, KBRL for technical support.

431

432 **Funding**

433 S.C. is supported by NIH/NCI/NIDA (DP2CA238295, R01CA231112, R33CA225498, RF1DA048811),
434 DoD (W81XWH-17-1-0235, W81XWH-20-1-0072, W81XWH-21-1-0514), Damon Runyon Dale Frey
435 Award (DFS-13-15), Melanoma Research Alliance (412806, 16-003524), Cancer Research Institute (CLIP),
436 AACR (17-20-01-CHEN), The V Foundation (V2017-022), Alliance for Cancer Gene Therapy, Sontag
437 Foundation (DSA), Pershing Square Sohn Cancer Research Alliance, Dexter Lu, Ludwig Family
438 Foundation, Blavatnik Family Foundation, and Chenevert Family Foundation. GW is supported by CRI
439 Irvington and RJ Anderson Postdoctoral Fellowships. RC is supported by NIH MSTP training grant
440 (T32GM007205) and NRSA fellowship (F30CA250249).

441

442 **Data and material availability**

443 All data generated or analyzed during this study are included in this article and its supplementary
444 information files. Source data and statistics are provided in an excel file of **Source data and statistics**.
445 Processed data for genomic sequencing and gene expression are provided as processed quantifications in

MUCIG Therapy

446 **Supplementary Datasets.** Genomic sequencing raw data are being deposited to NIH Sequence Read
447 Archive (SRA) and/or Gene Expression Omnibus (GEO), with pending accession numbers. Data, codes
448 and materials that support the findings of this research are available from the corresponding author upon
449 reasonable request to the academic community.

450

451

MUCIG Therapy

452 **Methods**

453

454 **Cell lines**

455 HEK293FT cell was purchased from ThermoFisher Scientific for producing viruses. All cell lines used in
456 this paper were maintained at 37C with 5% CO₂ in D10 medium (Dulbecco's modified Eagle's medium
457 supplemented with 10% fetal bovine serum).

458

459 **Mice**

460 Mice of both sexes, between age 6 and 12 weeks, were used for the study. 6-8-week-old C57BL/6Nr mice
461 were purchase from Charles River lab. Female mice were used for breast cancer (E0771) models. Male
462 mice were used for B16F10 and Pan02 mouse model. 6-8-week-old BALB/C mice were purchased from
463 Jackson lab, which were used for Colon26 mouse model. All animals were housed in standard, individually
464 ventilated, pathogen-free conditions, with a 12 h:12 h or a 13 h:11 h light cycle, at room temperature (21–
465 23 °C) and 40–60% relative humidity.

466

467 **Cas13d cancer cell line generation**

468 For lentivirus production, 20µg plasmid of PXR001 (EF1a-Cas13d-2A-EGFP, addgene#109049) together
469 with 10µg pMD2.G and 15µg psPAX2 were co-transfected into HEK293FT cells in a 150mm cell culture
470 dish at 80-90% confluency using 135µl LipoD293 transfection reagent (Signage, SL100668). Virus
471 supernatant was collected 48h post transfection, centrifuged at 3000g for 15min to remove the cell debris.
472 The supernatant was then concentrated with Amicon Ultra-15 filter from 20ml to 2ml. The virus was
473 aliquoted and stored at -80C. To generate Cas13d overexpression cell line, the cancer cells were transduced
474 with lentivirus PXR001, and the positive cells which were GFP expressing were flow cytometry sorted.

475

476 **Transfection and flow cytometry knockdown efficacy test**

477 To test each gRNA knockdown efficacy, gRNAs were cloned into BbsI site of PXR003 plasmid (Cas13d
478 gRNA cloning backbone, addgene#109053) and were transient transfected into Cas13d expressing cancer
479 cell. For the transfection experiments, 5x10⁴ cells per well of a 48 well plate was seeded 12h before
480 transfection. 500ng gRNA plasmid together with a 1:1 ratio of Lipofectamine 2000 to DNA were
481 transfected into cells. Flow cytometry was performed at 48h post transfection.

482

483 **Dual reporter cell line with Cas13d expressing generation**

MUCIG Therapy

484 A lentivirus version plasmid expressing Cas13d and blasticidin (EF1a-Cas13d-T2A-BSD-WPRE) was
485 cloned. A lentivirus version plasmid expressing U6_Direct repeats_guideRNA was cloned. E0711 cell line
486 was co-transduced with three lentiviruses (Cas13d-blasticidin, GFP and mCherry). The Cas13d-expressing
487 dual reporter E0771 cells was selected with blasticidin and then sorted with GFP⁺ mCherry⁺ double positive
488 cells. The dual reporter cells were then transduced with Cas13d-guideRNA lentivirus.

489

490 **Quantitative reverse transcription PCR (qRT-PCR)**

491 RNA was extracted by TRIzol (Invitrogen), and the cDNA was synthesized using the PrimeScript RT
492 master kit (Takara, RR036A). The qPCR was done using PowerUp SYBR Green Master Mix (Thermofisher)
493 following the instruction. The expression levels of genes were detected on QuantStudio™ 3 Real-Time
494 PCR System. The gene relative expression was calculated by the 2- $\Delta\Delta C_t$ method. GAPDH was measured
495 as reference.

496

497 **Generation of AAV-MUCIG pools**

498 An AAV version plasmid expressing U6-mutation direct repeat-gRNA clone site-EFS-Cas13d (pAAV-U6-
499 EFS-Cas13d) was cloned into AAV backbone. All pooled gRNA library were synthesized as single
500 stranded oligonucleotides from Genescript or IDT. The oligos were amplified by PCR and Gibson cloned
501 into pAAV-U6-EFS-Cas13d. The purification and electroporation of Gibson products into Endura
502 electrocompetent cells were performed as previously described(Joung et al., 2017), with at least x100
503 coverage of colonies represented per sgRNAs. AAV was produced by co-transfecting HEK293FT cells
504 with AAV-MUCIG pool together with AAV9 serotype plasmid and helper plasmid PDF6. Briefly,
505 HEK293FT cells were seeded in 150cm dish or hyper flask 12-18h before transfection. When cells got 80-
506 90% confluency, 6.2 μ g AAV-vector or AAV-MUCIG pool, 8.7 μ g AAV9 serotype, and 10.4 μ g PDF6 were
507 transfected with 130 μ l PEI, incubating 10-15min before adding into cells. Replicates collected multiple
508 dishes were pooled to enhance production yield. Cells were collected 72h post transfection. For AAV
509 purification, chloroform (1:10 by volume) was added and was shaken vigorously for 1h at 37°C. NaCl was
510 added to a final concentration of 1M and shaken until dissolved. The mixture was centrifuges at 20,000g
511 for 15min at 4°C. The aqueous layer was transferred to a new tube, and then PEG 8000 (10%, w/v) was
512 added and shaken until dissolved. The mixture was incubated on ice for 1h. The pellet was spun down at
513 20,000g for 15min at 4°C. The supernatant was discarded, and the pellet was resuspended in DPBS. The
514 resuspension was treated with Benzonase and MgCl₂ AT 37C for 30min. Chloroform (1:1 by volume) was
515 then added, shaken and spun down at 12,000g for 15min at 4°C. The aqueous layer was isolated and
516 concentrated through Ambion Ultra-15 tube. The concentrated solution was washed with PBS and the

MUCIG Therapy

517 filtration process repeated. Then AAV was treated with DNase I for 30min at 37°C. Genomic copy number
518 (GC) of AAV was determined by real-time qPCR using custom TaqMan assays (Thermo Fisher Scientific)
519 targeted to EFS promoter.

520

521 **Therapeutic testing of AAV-MUCIG in syngeneic tumor models**

522 Syngeneic orthotopic breast tumor was established by transplanting 2×10^6 E0771 cells into mammary fat
523 pad of 6–8-week-old female C57BL/6Nr mice. Then 5, 9, and 14 days after transplantation, 2×10^{11} AAV
524 partials of vector or MUCIG, or PBS were injected intratumorally into tumor bearing mice. The tumor
525 volume was measured every 3-4 days. For the B16F10 melanoma model, 1×10^6 B16F10 cancer cells were
526 subcutaneously injected into the male left flank of C57BL/6Nr mice. 5, 9, 13 days post transplantation, 2×10^{11}
527 AAV partials of vector or MUCIG, or PBS were intratumorally administrated into tumor bearing mice. The
528 tumor volume was measured every 2 days. For the pancreatic tumor model, 2×10^6 Pan02 cells were
529 subcutaneously injected into the left flank of C57BL/6Nr mice. Then, 5, 14, 18 days after transplantation,
530 2×10^{11} AAV partials of vector or MUCIG, or PBS were intratumorally administrated into tumor bearing mice.
531 The tumor volume was measured every 3-4 days. For the colon tumor model, 2×10^6 Colon26 cells were
532 subcutaneously injected into the left flank of BALB/C mice. Then, 5, 9, 14 days after transplantation, 2×10^{11}
533 AAV partials of vector or MUCIG, or PBS were intratumorally administrated into tumor bearing mice. The
534 tumor volume was measured every 3 days. Tumor volume was calculated with the formula: volume =
535 $\pi/6 \times xyz$. Two-way ANOVA was used to compare growth curves between treatment groups.

536

537 **Therapeutic testing of AAV-PGGC in E0771 dual sites tumor model**

538 The E0771 breast cancer dual site model was established by transplanting 2×10^6 E0771 cells into left and
539 0.2×10^6 E0771 cells into the right mammary fat pad of 8-week-old female C57BL/6Nr mice. Then 5, 8, 11,
540 14 and 18 days after transplantation, 2×10^{11} AAV partials of vector or PGGC, or PBS per dose were injected
541 intratumorally into the primary site of tumor bearing mice. The tumor volume was measured every 3-4 days.
542 Tumor volume was calculated with the formula: volume = $\pi/6 \times xyz$. Two-way ANOVA was used to
543 compare growth curves between treatment groups.

544

545 **Therapeutic testing of AAV-PGGC in lung metastasis tumor model**

546 8-week-old female C57BL/6 mice were orthotopically injected with 2×10^6 E0771 or E0771-luciferse
547 expressing cells, and then a day later intravenous (IV) injection of 0.2×10^6 E0771-luciferse expressing cells.
548 Then 5, 8, 12, 15 and 18 days after transplantation, mice were intratumorally and intravenously injected
549 with AAV-Vector or AAV-PGGC, and intraperitoneally (IP) treated with 100ug per dose of isotype or anti-

MUCIG Therapy

550 Gr1 antibody at the indicated time points. The primary tumor volume was measured every 3-4 days. Tumor
551 volume was calculated with the formula: $\text{volume} = \pi/6 * xyz$. Two-way ANOVA was used to compare
552 growth curves between treatment groups. Lung metastasis progression was measured by bioluminescent
553 imaging using IVIS every 3 days. Survival curves were analyzed by Log-rank (Mantel-Cox) test.

554

555 ***In vivo* luciferase imaging**

556 The bioluminescent imaging was performed to detect AAV delivery gene expression. Mice were injected
557 with luciferin (150mg/kg) by intraperitoneal injection and activity quantified in live animal for 10min later
558 following with 1min exposure. The photon flux was monitored by the PE IVIS Spectrum in vivo imaging
559 system. The signaling was monitored and quantified by the IVIS software.

560

561 **Isolation of TILs**

562 Tumors were minced into 1 mm size pieces and then digested with 100U/ml collagenase IV and DNase I
563 for 60min at 37°C. Tumor suspensions were filtered through 100- μm cell strainer to remove large bulk
564 masses. The cells were washed twice with wash buffer (PBS plus 2% FBS). 1ml ACK lysis buffer was
565 added to lysis red blood cell by incubating 2-5 min at room temperature. The suspension was then diluted
566 with wash buffer and spin down at 400g for 5min at 4°C. Cell pellet was resuspended with wash buffer and
567 followed by passing through a 40 μm cell strainer. Cells were spin down and washed twice with wash buffer.
568 At last, cell pellet was resuspended in MACS buffer (PBS with 0.5% BSA and 2mM EDTA). The single
569 cell suspensions were used for flow cytometry staining and FACS sorting. TILs were labeled as CD45
570 positive cells.

571

572 **Flow cytometry**

573 For the TILs flow cytometry analysis, single cell suspension from tumor were prepared as described above.
574 For the myeloid cell staining panel, anti-CD45-Percp-Cy5.5, anti-CD11b-FITC, anti-CD11c-PE/Dazzle,
575 anti-F4/80-PE, anti-Ly6G-BV605, anti-Ly6C-APC, and anti-MHCII-PE/Cy7 were used. For lymphoid cell
576 staining panel, anti-CD45-Percp-Cy5.5, anti-CD8-BV605, anti-CD4-PE. All flow antibodies were used at
577 1:100 dilutions for staining. The LIVE/DEAD Near-IR was diluted 1:1000 to distinguish live or dead cells.

578

579 For the in vitro cancer cell line staining, cancer cells were incubated with trypsin and washed twice with
580 PBS. For cell surface staining, surface antibody was diluted 1:100 and stained in MACS buffer on ice for
581 15min. Cells were washed twice with MACS buffer. For intracellular staining, Intracellular Fixation &
582 Permeabilization Buffer Set (eBioscience) was used to fix and permeabilize cells. Briefly, after the surface

MUCIG Therapy

583 marker staining, cells were resuspended in 100 μ l Fixation/Permeabilization working solution, and
584 incubated on ice for 15 min. Then cells were washed with 1 \times permeabilization buffer by centrifugation at
585 600g for 5 min. Then the cell pellet was resuspended in 100 μ l of 1 \times permeabilization buffer with 1:100
586 intracellular staining antibodies and incubating on ice for 15min. After staining, cells were centrifuged at
587 600g for 5 min, and washed twice with staining buffer before being analyzed or sorted on a BD FACSAria.
588 The data were analyzed using FlowJo software.

589

590 **Immune cell profiling by scRNA-seq**

591 E0771 or Colon26 tumors were collected at the indicated time point post injection. Single cell suspensions
592 were collected as described above. The cells were labeled with CD45-Percp-Cy5.5 antibody and live/dead
593 dye. FACS sorted cells were gated on CD45⁺ live cells. Sorted cells were washed with PBS, and cell
594 numbers and viabilities were assessed by trypan blue staining. The 10,000 CD45⁺ cells isolated from tumors
595 were used for scRNA-seq library prep by following the protocol from 10x Genomics Chromium Next GEM
596 Single Cell 5' Reagent Kits V2.

597

598 **scRNA-seq data analysis**

599 Analysis of scRNA-seq was performed using the Seurat v4 package in R. All cells from the three treatment
600 groups (PBS, AAV-Vector, and AAV-PGGC) were merged and integrated by tumor type (E0771 or
601 Colon26). The data was filtered to retain cells with < 15% mitochondrial counts and 200-3500 unique
602 expressed features. The expression data for each cell was normalized by the total reads and log- transformed.
603 We utilized Harmony to integrate datasets from the same tumor type for the purpose of identifying cell
604 clusters. Each cell cluster was annotated by cell type using canonical marker genes, with higher-resolution
605 subclustering of the lymphocyte populations. To determine differences in cell type frequencies, we
606 constructed 2x2 contingency tables for each cell type, comparing AAV-Vector and AAV-PGGC treatment
607 groups. A two-tailed Fisher's exact test was performed on the contingency table for each cell type.
608 Differentially expressed genes were identified by comparing cells from AAV-Vector vs AAV-PGGC
609 treatment groups using the default settings in Seurat, with statistical significance set at adjusted $p < 0.05$.

610

611 **Statistical analysis**

612 Standard non-NGS statistical analyses were performed in GraphPad Prism using specific statistical tests
613 where appropriate, as detailed in figure legends. NGS statistical analyses were performed in R/RStudio.
614 Different levels of statistical significance were accessed based on specific p values and type I error cutoffs
615 (e.g. 0.05, 0.01, 0.001, 0.0001).

MUCIG Therapy

616 **Figure Legends**

617

618 **Figure 1. Multiplexed Cas13d repression of immunosuppressive genes as combinatorial cancer**
619 **immunotherapy**

620 **A.** Schematics of the experimental design for evaluating Multiplex Universal Combinatorial
621 Immunotherapy via Gene-silencing (MUCIG) as immunotherapy. Top, design of the MUCIG Vector,
622 which is an all-in-one AAV vector that contains an EFS-driven Cas13d expression cassette and a U6-driven
623 Cas13d guide RNA cassette.

624 **B.** Design of four different gRNA libraries targeting immunosuppressive gene combinations.

625 **C.** Growth curves of E0771 tumors in C57BL/6 mice. 2×10^6 E0771 cells were orthotopically injected into
626 C57BL/6 mice. Mice were intratumorally injected with PBS (n = 9), AAV-MUCIG-Vector (Cas13d) (n =
627 10), AAV-MUCIG Pool1 (n = 9), Pool2 (n = 9), Pool3 (n = 9), or Pool4 (n = 10) at days 5, 9 and 14 with
628 2×10^{11} AAV per dose.

629 **D.** Spider plots of (C) separated by treatment group for visibility.

630 Data points in this figure are presented as mean \pm s.e.m. Statistical significance was assessed by two-way
631 ANOVA. * $p < 0.05$, ** $p < 0.01$, *** $p < 0.001$, **** $p < 0.0001$. Non-significant comparisons not shown.

632 **See also: Figures S1-S4**

633

634 **Figure 2. Rational optimization of MUCIG generates AAV-PGGC, an effective four-gene**
635 **combination immunotherapy**

636 **A-D.** Protein-level characterization of a list of immunosuppressive factors across a panel of syngeneic
637 cancer cell lines. Heat maps detailing surface (A) and intracellular (B) expression of all assayed
638 immunosuppressive factors determined by flow cytometry. Data are expressed in terms of the percentage
639 of total cells that express each marker.

640 **C&D.** Flow cytometry analysis of PGGC pool targets (PDL1, GALECTIN9, GALECTIN3, and CD47) in
641 different murine cancer cell lines, either by surface (C) or intracellular (D) staining.

642 **E.** Flow cytometry analysis of PGGC pool targets *in vivo* from syngeneic E0771 tumors. C57BL/6 mice (n
643 = 3) were orthotopically injected with 2×10^6 E0771-GFP cells. The tumors were harvested at 23 days post
644 injection. Tumor tissues were dissociated for flow cytometry analysis of the indicated markers in each
645 compartment.

646 **F.** Schematics of the experimental design for intratumoral delivery of the four-gene AAV-PGGC cocktail.

MUCIG Therapy

647 **G.** Growth curves of orthotopic E0771 tumors in C57BL/6 mice. Mice were intratumorally injected with
648 AAV-Vector (Cas13d) (n = 10), AAV-MUCIG Pool4 (n = 5), and AAV-PGGC (n = 10) at days 5, 9 and
649 14 with $2e^{11}$ AAV per dose.

650 **H.** Spider plots of (C), separated by treatment group for visibility.

651 Data points in this figure are presented as mean \pm s.e.m. Statistical significance was assessed by two-way
652 ANOVA. *** $p < 0.001$, **** $p < 0.0001$. Non-significant comparisons not shown.

653

654 **Figure 3. AAV-PGGC therapy demonstrates broader anti-tumor activity in syngeneic models of**
655 **different cancer types**

656 **A.** Melanoma model. C57BL/6 mice were subcutaneously injected with $1e^6$ B16F10 melanoma cells.
657 Growth curves of B16F10 tumors intratumorally treated with PBS (n = 5), AAV-Vector (n = 5), AAV-
658 MUCIG Pool4 (n = 5), and AAV-PGGC (n = 5) ($2e^{11}$ AAV per dose) at the timepoints indicated by black
659 arrowheads.

660 **B.** Spider plots of growth curves in (A), separated for visibility.

661 **C.** Colon cancer model. BALB/C mice were subcutaneously injected with $2e^6$ Colon26 colon cancer cells.
662 Growth curves of Colon26 tumors intratumorally injected with PBS (n = 5), AAV-Vector (n = 5), AAV-
663 MUCIG Pool4 (n = 5), and AAV-PGGC (n = 5) ($2e^{11}$ AAV per dose) at the timepoints indicated by black
664 arrowheads.

665 **D.** Spider plots of growth curves in (C), separated for visibility.

666 **E.** Pancreatic cancer model. C57BL/6 mice were subcutaneously injected with $2e^6$ Pan02 pancreatic cancer
667 cells. Growth curves of Pan02 tumors intratumorally treated with PBS (n = 5), AAV-Vector (n = 5), AAV-
668 MUCIG Pool4 (n = 5), and AAV-PGGC (n = 5) ($2e^{11}$ AAV per dose) at the timepoints indicated by black
669 arrowheads.

670 **F.** Spider plots of growth curves in (E), separated for visibility.

671 Data points in this figure are presented as mean \pm s.e.m. Statistical significance was assessed by two-way
672 ANOVA. ** $p < 0.01$, **** $p < 0.0001$. Non-significant comparisons not shown.

673

674 **Figure 4. AAV-PGGC treatment remodels the immunosuppressive tumor microenvironment.**

675 **A.** Schematic of experimental design for analyzing of the composition of tumor infiltrating immune
676 populations after AAV-PGGC therapy.

677 **B.** Relative abundances of several immune populations in orthotopic E0771 (top panels) and subcutaneous
678 Colon26 (bottom panels) tumors, at the endpoint of tumor study (35 days post tumor induction). For the
679 E0771 model, mice were intratumorally treated with PBS (n = 3), AAV-Vector (n = 4) or AAV-PGGC (n

MUCIG Therapy

680 = 4) at days 4, 9 and 14. For the Colon26 model, mice were intratumorally treated with PBS (n = 4), AAV-
681 Vector (n = 4) or AAV-PGGC (n = 4) at days 4, 9 and 14. Statistical significance was assessed by one-way
682 ANOVA Tukey's multiple comparisons test, adjusted P Value. (* $p < 0.05$, ** $p < 0.01$, *** $p < 0.001$).
683 Non-significant comparisons not shown.

684 **C.** UMAP visualization of single tumor-infiltrating immune cells, profiled by scRNA-seq. Mice bearing
685 orthotopic E0771 tumors were treated with PBS, AAV-Vector or AAV-PGGC at days 4, 9 and 14. Tumors
686 were harvested at day 29, and live CD45⁺ cells were sorted for scRNA-seq.

687 **D.** Violin plots showing the expression levels of representative marker genes across the main cell clusters.

688 **E.** Relative proportions of each cell type, across treatment groups. Statistical analysis between groups was
689 performed by two-tailed Fisher's exact test.

690 **F.** UMAP visualization of single tumor-infiltrating immune cells, profiled by scRNA-seq. Mice bearing
691 subcutaneous Colon26 tumors were treated with PBS, AAV-Vector or AAV-PGGC at days 4, 9 and 14.
692 Tumors were harvested at day 29, and live CD45⁺ cells were sorted for scRNA-seq.

693 **G.** Violin plots showing the expression levels of representative marker genes across the main cell clusters.

694 **H.** Relative proportions of each cell type, across treatment groups. Statistical analysis between groups was
695 performed by two-tailed Fisher's exact test.

696 **See also: Figure S5**

697

698 **Figure 5. AAV-PGGC therapy is dependent on CD8⁺ T cells and inhibited by suppressive immune**
699 **cells in the tumor microenvironment**

700 **A.** Schematic of experimental design for AAV-PGGC and antibody treatment. C57BL/6 mice were
701 orthotopically injected with 2x10⁶ E0771 cells. Mice were intratumorally injected with AAV-Vector or
702 AAV-PGGC at the indicated timepoint. The tumor bearing mice were intraperitoneally (IP) treated with
703 100ug per dose of isotype control, anti-CD8 or anti-GR1 antibody at the indicated time points.

704 **B.** Growth curves of orthotopic E0771 tumors in C57BL/6 mice after different combinations of AAV with
705 antibodies.

706 **C&D.** Plot split from B. Analysis of specific CD8⁺ T cell (C) or MDSC/neutrophil (D) depletion on AAV-
707 PGGC treatment.

708 Data points in this figure are presented as mean ± s.e.m. Statistical significance was assessed by two-way
709 ANOVA. * $p < 0.05$, *** $p < 0.001$, **** $p < 0.0001$. Non-significant comparisons not shown.

710

711 **Figure 6. AAV-PGGC treatment inhibits metastatic cancer and extends survival**

MUCIG Therapy

712 **A.** Schematic of experimental design for a dual site tumor model. C57BL/6 mice were orthotopically
713 injected with 2×10^6 E0771 cells at left and 0.2×10^6 E0771 cells at right fat pad. Mice were intratumorally
714 injected with AAV-Vector or AAV-PGGC (2×10^{11} AAV per dose) at the indicated timepoint only at the left
715 site.

716 **B&C.** Growth curves of primary tumor site (B) and distant tumor site (C) in C57BL/6 mice after AAV-
717 PGGC treatment. Statistical significance was assessed by two-way ANOVA.

718 **D.** Schematic of experimental design for E0771 orthotopic tumor and lung distant metastasis model.
719 C57BL/6 mice were orthotopically injected with 2×10^6 E0771-luciferase expressing cells, and a day later
720 intravenous (IV) injection of 0.2×10^6 E0771-luciferase expressing cells. Mice were intratumorally and
721 intravenously injected with AAV-Vector or AAV-PGGC (4×10^{11} AAV per dose), and intraperitoneally
722 (IP) treated with 100ug per dose of isotype or anti-Gr1 antibody at the indicated time points.

723 **E.** Growth curves of primary tumor in C57BL/6 mice after AAV-PGGC plus anti-Gr1 antibody treatment.
724 Statistical significance was assessed by two-way ANOVA.

725 **F.** Lung metastatic progression was measured by bioluminescent imaging using IVIS.

726 **G.** Lung metastasis free survival. The metastasis free survival is defined by the luciferase signal when first
727 showed up in the lung. To standardize across mice, the luciferase signal was firstly normalized from min
728 500 to max 70,000, then the lung luciferase signal was checked whether showed up or not. Survival curves
729 were analyzed by Log-rank (Mantel-Cox) test.

730 **H.** Overall survival. Survival curves were analyzed by Log-rank (Mantel-Cox) test.

731 Data points in this figure are presented as mean \pm s.e.m. Statistical significance was assessed by two-way
732 ANOVA, or Log-rank test as indicated in each panel. * $p < 0.05$, ** $p < 0.01$, *** $p < 0.001$, **** $p <$
733 0.0001 . Non-significant comparisons not shown.

734 **See also: Figure S6**

735

736

737 **Supplemental Figures**

738

739 **Figure S1. Identification of efficient Cas13d gRNAs against *Pd11* and *Galectin9***

740 **A.** Schematic of the experimental approach to identify efficient gRNAs targeting *Pd11* and *Galectin9*.
741 Hepa1-6 tumor cells were transduced with Cas13d-EGFP lentivirus. Then GFP⁺ cells were sorted and
742 transfected with gRNA plasmids. Two days after transfection, target gene expression was tested by flow
743 cytometry analysis.

744 **B.** Target sites of the 40 Cas13d gRNAs located along the *Pd11* transcript.

MUCIG Therapy

745 **C&D.** Flow cytometry analysis of PDL1(C) and GALECTIN9 (D) knockdown efficacy by Cas13d-gRNAs.
746 The gRNA with the highest knockdown efficacy is highlighted in red. Data are expressed as the relative
747 mean of fluorescent intensity (MFI). The gene expression level of Vector was normalized to 1.

748 **Related to: Figure 1**

749

750 **Figure S2. Cas13d-mediated silencing of endogenous immunosuppressive genes in cancer cells**

751 **A.** Schematic of the experimental approach to identify efficient Cas13d gRNAs targeting various
752 immunosuppressive genes. The all-in-one plasmid including gRNA, Cas13 and EGFP was transfected into
753 Hepa1-6 or MC38 cells. Two days after transfection, target gene expression was tested by flow cytometry
754 analysis. The gRNA successful transfected cells were gated by GFP⁺ cells.

755 **B.** Knockdown efficiency of gRNAs targeting different immunosuppressive genes in cancer cell lines.
756 CD47 and GALECTIN3 were tested in Hepa1-6 cells, and CD66a and CD200 were tested in MC38 cells.
757 Data are expressed as the relative mean of fluorescent intensity (MFI). The gene expression level of vector
758 group was normalized to 1.

759 **C.** Schematic of the experimental approach to compare the knockdown efficient of wild type director repeat
760 (WT-DR) and mutant (Mut-DR). E0771 tumor cells were transduced with Cas13d-EGFP lentivirus. Then
761 GFP⁺ cells were sorted and transfected with WT-DR gRNA or Mut-DR gRNA plasmids. Two days after
762 transfection, target gene expression was tested by flow cytometry analysis.

763 **D.** Comparison of WT-DR and mut-DR knockdown efficiency when targeting PDL1 and CD73 in E0771
764 cells. Data are expressed as the relative mean of fluorescent intensity (MFI). The gene expression level of
765 WT-DR group was normalized to 1.

766 **E.** Schematic of the experimental approach to compare knockdown efficient between Cas13d gRNAs and
767 shRNA. The cas13d all-in-one (gRNA-Cas13-EGFP) or shRNA plasmid was transfected into Hepa1-6 or
768 MC38 cells. Two days after transfection, target gene expression was tested by flow cytometry analysis. The
769 gRNA successful transfected cells were gated by GFP⁺ cells.

770 **F.** Comparison of the Cas13d gRNA-mediated and shRNA-mediated target knockdown. CD47 and
771 GALECTIN3 were tested in Hepa1-6 cells, and CD66a and CD200 were tested in MC38 cells. Data are
772 expressed as the relative mean of fluorescent intensity (MFI). The gene expression level of vector group
773 was normalized to 1.

774 Data points in this figure are presented as mean \pm s.e.m. Statistical significance was assessed by two-tailed
775 unpaired *t* test. * $p < 0.05$, ** $p < 0.01$, *** $p < 0.001$, **** $p < 0.0001$. Non-significant comparisons not
776 shown.

777 **Related to: Figure 1**

MUCIG Therapy

778

779 **Figure S3. Cas13d on-target and collateral activity testing when targeting endogenous**
780 **immunosuppressive genes**

781 **A.** Diagram of Cas13d collateral activity and on-target activity by a dual-GFP and mCherry reporter system.
782 E0711 cell line was co-transduced with three lentiviruses (Cas13d-blasticidin, GFP and mCherry). The
783 Cas13d-expressing dual reporter E0771 cells was selected with blasticidin and then sorted by GFP⁺
784 mCherry⁺ double positive cells. The dual reporter cells were then transduced with Cas13d-guideRNA
785 lentivirus. Then the GFP and mCherry fluorescent signal was determined by flow cytometry. The on-target
786 gene expression was tested by flow cytometry and qPCR.

787 **B.** Flow cytometry analysis of E0771 dual-reporter cells after transduced with different guide RNAs. NTC
788 (Non-Transduced-Control), EV (Empty Vector), SCRG(scramble guideRNA).

789 **C.** RT-qPCR analysis of the target gene expression. The gene mRNA expression level of SCRG was
790 normalized to 1. Data points in this figure are presented as mean \pm s.e.m. Statistical significance was
791 assessed by one-way ANOVA Tukey's multiple comparisons test, adjusted P Value. Multiple comparisons
792 were summarized in the bellowing table. * $p < 0.05$, ** $p < 0.01$, *** $p < 0.001$.

793 **Related to: Figure 1**

794

795 **Figure S4. Persistent ectopic gene expression in tumors after intratumoral AAV injection**

796 C57BL/6 mice were orthotopically injected with 2×10^6 E0771 cells. AAV-luciferase-GFP was then
797 intratumorally injected at the indicated time points. In vivo bioluminescence imaging was performed to
798 visualize luciferase activity.

799 **Related to: Figure 1**

800

801 **Figure S5. Tumor infiltrating immune population analysis and common signatures of downregulated**
802 **genes in immune cell populations upon AAV-PGGC treatment**

803 **A.** The gating strategy for myeloid and lymphocyte cells flow cytometry staining panels are shown. Arrows
804 indicate the parent population that the subsequent plot is gated on. CD8⁺ T = CD8⁺CD45⁺, CD4⁺ =
805 CD4⁺CD45⁺, Macrophage = CD11b⁺F4/80⁺, Dendric cell (DC) = CD11c⁺MHCII⁺, MDSC =
806 CD11b⁺Ly6G⁺(PMN-MDSC) + CD11b⁺Ly6C⁺(M-MDSC).

807 **B-D.** Overlap of the down-regulated genes in CD8⁺ T cells (**B**), neutrophils (**C**) and macrophages (**D**),
808 comparing AAV-PGGC vs AAV-Vector (Cas13d) in both the Colon26 and E0771 tumor models.

809 **Related to: Figure 4**

810

MUCIG Therapy

811

812 **Figure S6. AAV-PGGC local treatment moderately inhibits lung metastasis**

813 **A.** Schematic of experimental design for E0771 orthotopic tumor and lung distant metastasis model.

814 C57BL/6 mice were orthotopically injected with 2×10^6 E0771-luciferase expressing cells, and a day later

815 0.2×10^6 E0771-luciferase expressing cells were intravenously (I.V.) injected. Then mice were intratumorally

816 injected with AAV-Vector or AAV-PGGC (2×10^{11} AAV per dose) at the indicated time points.

817 **B.** Growth curves of primary tumor in C57BL/6 mice after AAV-PGGC treatment.

818 **C.** Lung metastatic progression was measured by bioluminescent imaging using IVIS. Representative IVIS

819 imaging are shown.

820 **D.** Lung metastatic free survival. The metastasis free survival is defined by the luciferase signal when first

821 showed up in the lung. To standardize across mice, the luciferase signal was firstly normalized from min

822 100 to max 10,000, then the lung luciferase signal was checked whether showed up or not. Survival curves

823 were analyzed by Log-rank (Mantel-Cox) test.

824 **E.** Overall survival. Survival curves were analyzed by Log-rank (Mantel-Cox) test.

825 Data points in this figure are presented as mean \pm s.e.m. Statistical significance was assessed by two-way

826 ANOVA, or Log-rank test as indicated in each panel. * $p < 0.05$, *** $p < 0.001$. Non-significant

827 comparisons not shown.

828 **Related to: Figure 6**

829

830

MUCIG Therapy

831 **Other Supplemental Files**

832

833 **Key Resources Table**

834 Key resource information is provided in a table.

835

836 **DNA oligonucleotide sequence information**

837 All oligo sequences used in this study were listed in an excel file.

838

839 **Dataset S1 - Source data and statistics**

840 Source data and statistics of non-NGS type data are provided in an excel file.

841

842 **Dataset S2 - NGS data**

843 Processed data and statistics of NGS data are provided in an excel file.

844

845

846

847

MUCIG Therapy

848

849 **References**

850

851 Baghban, R., Roshangar, L., Jahanban-Esfahlan, R., Seidi, K., Ebrahimi-Kalan, A., Jaymand, M., Kolahian, S.,
852 Javaheri, T., and Zare, P. (2020). Tumor microenvironment complexity and therapeutic implications at a glance. *Cell*
853 *Commun Signal* 18, 59.

854 Binnewies, M., Roberts, E. W., Kersten, K., Chan, V., Fearon, D. F., Merad, M., Coussens, L. M., Gabrilovich, D. I.,
855 Ostrand-Rosenberg, S., Hedrick, C. C., *et al.* (2018). Understanding the tumor immune microenvironment (TIME)
856 for effective therapy. *Nat Med* 24, 541-550.

857 Biswas, S., Guix, M., Rinehart, C., Dugger, T. C., Chytil, A., Moses, H. L., Freeman, M. L., and Arteaga, C. L. (2007).
858 Inhibition of TGF-beta with neutralizing antibodies prevents radiation-induced acceleration of metastatic cancer
859 progression. *J Clin Invest* 117, 1305-1313.

860 Boettcher, M., and McManus, M. T. (2015). Choosing the Right Tool for the Job: RNAi, TALEN, or CRISPR. *Mol*
861 *Cell* 58, 575-585.

862 Buchbinder, E. I., and Desai, A. (2016). CTLA-4 and PD-1 Pathways: Similarities, Differences, and Implications of
863 Their Inhibition. *Am J Clin Oncol* 39, 98-106.

864 Chang, A. L., Miska, J., Wainwright, D. A., Dey, M., Rivetta, C. V., Yu, D., Kanojia, D., Pituch, K. C., Qiao, J.,
865 Pytel, P., *et al.* (2016). CCL2 Produced by the Glioma Microenvironment Is Essential for the Recruitment of
866 Regulatory T Cells and Myeloid-Derived Suppressor Cells. *Cancer Res* 76, 5671-5682.

867 Deyle, D. R., and Russell, D. W. (2009). Adeno-associated virus vector integration. *Curr Opin Mol Ther* 11, 442-
868 447.

869 Gabrilovich, D. I., and Nagaraj, S. (2009). Myeloid-derived suppressor cells as regulators of the immune system. *Nat*
870 *Rev Immunol* 9, 162-174.

871 Gómez-Herranz, M., Nekulova, M., Faktor, J., Hernychova, L., Kote, S., Sinclair, E. H., Nenutil, R., Vojtesek, B.,
872 Ball, K. L., and Hupp, T. R. (2019). The effects of IFITM1 and IFITM3 gene deletion on IFN γ stimulated protein
873 synthesis. *Cell Signal* 60, 39-56.

874 Granados-Riveron, J. T., and Aquino-Jarquín, G. (2018). CRISPR-Cas13 Precision Transcriptome Engineering in
875 Cancer. *Cancer Res* 78, 4107-4113.

876 Grzywa, T. M., Sosnowska, A., Matryba, P., Rydzynska, Z., Jasinski, M., Nowis, D., and Golab, J. (2020). Myeloid
877 Cell-Derived Arginase in Cancer Immune Response. *Front Immunol* 11, 938.

878 Haabeth, O. A. W., Blake, T. R., McKinlay, C. J., Tveita, A. A., Sallets, A., Waymouth, R. M., Wender, P. A., and
879 Levy, R. (2019). Local Delivery of Ox40l, Cd80, and Cd86 mRNA Kindles Global Anticancer Immunity. *Cancer*
880 *Res* 79, 1624-1634.

881 Hammers, H., Plimack, E. R., Infante, J. R., Ernstoff, M., Rini, B. I., McDermott, D. F., Razak, A., Pal, S. K., Voss,
882 M., Sharma, P., *et al.* (2014). Phase I Study of Nivolumab in Combination with Ipilimumab in Metastatic Renal Cell
883 Carcinoma (Mrcc). *Annals of Oncology* 25.

884 Hao, N. B., Lu, M. H., Fan, Y. H., Cao, Y. L., Zhang, Z. R., and Yang, S. M. (2012). Macrophages in tumor
885 microenvironments and the progression of tumors. *Clin Dev Immunol* 2012, 948098.

MUCIG Therapy

- 886 Ishizuka, J. J., Manguso, R. T., Cheruiyot, C. K., Bi, K., Panda, A., Iracheta-Vellve, A., Miller, B. C., Du, P. P., Yates,
887 K. B., Dubrot, J., *et al.* (2019). Loss of ADAR1 in tumours overcomes resistance to immune checkpoint blockade.
888 *Nature* *565*, 43-48.
- 889 Jiang, Y., Li, Y., and Zhu, B. (2015). T-cell exhaustion in the tumor microenvironment. *Cell Death Dis* *6*, e1792.
- 890 Joung, J., Konermann, S., Gootenberg, J. S., Abudayyeh, O. O., Platt, R. J., Brigham, M. D., Sanjana, N. E., and
891 Zhang, F. (2017). Genome-scale CRISPR-Cas9 knockout and transcriptional activation screening. *Nat Protoc* *12*,
892 828-863.
- 893 Kelley, C. P., Haerle, M. C., and Wang, E. T. (2021). Negative autoregulation mitigates collateral RNase activity of
894 repeat-targeting CRISPR-Cas13d in mammalian cells. *bioRxiv*, 2021.2012.2020.473384.
- 895 Kim, R., Emi, M., Tanabe, K., and Arihiro, K. (2006). Tumor-driven evolution of immunosuppressive networks
896 during malignant progression. *Cancer Res* *66*, 5527-5536.
- 897 Konermann, S., Lotfy, P., Brideau, N. J., Oki, J., Shokhirev, M. N., and Hsu, P. D. (2018). Transcriptome Engineering
898 with RNA-Targeting Type VI-D CRISPR Effectors. *Cell* *173*, 665-676 e614.
- 899 Kong, Y., Zhu, L., Schell, T. D., Zhang, J., Claxton, D. F., Ehmann, W. C., Rybka, W. B., George, M. R., Zeng, H.,
900 and Zheng, H. (2016). T-Cell Immunoglobulin and ITIM Domain (TIGIT) Associates with CD8+ T-Cell Exhaustion
901 and Poor Clinical Outcome in AML Patients. *Clin Cancer Res* *22*, 3057-3066.
- 902 Lawson, K. A., Sousa, C. M., Zhang, X., Kim, E., Akthar, R., Caumanns, J. J., Yao, Y., Mikolajewicz, N., Ross, C.,
903 Brown, K. R., *et al.* (2020). Functional genomic landscape of cancer-intrinsic evasion of killing by T cells. *Nature*
904 *586*, 120-126.
- 905 Manguso, R. T., Pope, H. W., Zimmer, M. D., Brown, F. D., Yates, K. B., Miller, B. C., Collins, N. B., Bi, K., LaFleur,
906 M. W., Juneja, V. R., *et al.* (2017). In vivo CRISPR screening identifies Ptpn2 as a cancer immunotherapy target.
907 *Nature* *547*, 413-418.
- 908 Motz, G. T., and Coukos, G. (2013). Deciphering and reversing tumor immune suppression. *Immunity* *39*, 61-73.
- 909 Munn, D. H., and Bronte, V. (2016). Immune suppressive mechanisms in the tumor microenvironment. *Curr Opin*
910 *Immunol* *39*, 1-6.
- 911 Ni, G., Zhang, L., Yang, X., Li, H., Ma, B., Walton, S., Wu, X., Yuan, J., Wang, T., and Liu, X. (2020). Targeting
912 interleukin-10 signalling for cancer immunotherapy, a promising and complicated task. *Hum Vaccin Immunother* *16*,
913 2328-2332.
- 914 Pardoll, D. M. (2012). The blockade of immune checkpoints in cancer immunotherapy. *Nat Rev Cancer* *12*, 252-264.
- 915 Rabinovich, G. A., Gabrilovich, D., and Sotomayor, E. M. (2007). Immunosuppressive strategies that are mediated
916 by tumor cells. *Annu Rev Immunol* *25*, 267-296.
- 917 Ribeiro Franco, P. I., Rodrigues, A. P., de Menezes, L. B., and Pacheco Miguel, M. (2020). Tumor microenvironment
918 components: Allies of cancer progression. *Pathol Res Pract* *216*, 152729.
- 919 Rotte, A. (2019). Combination of CTLA-4 and PD-1 blockers for treatment of cancer. *J Exp Clin Cancer Res* *38*, 255.
- 920 Ru, B., Wong, C. N., Tong, Y., Zhong, J. Y., Zhong, S. S. W., Wu, W. C., Chu, K. C., Wong, C. Y., Lau, C. Y., Chen,
921 I., *et al.* (2019). TISIDB: an integrated repository portal for tumor-immune system interactions. *Bioinformatics* *35*,
922 4200-4202.

MUCIG Therapy

- 923 Sharma, P., Hu-Lieskovan, S., Wargo, J. A., and Ribas, A. (2017). Primary, Adaptive, and Acquired Resistance to
924 Cancer Immunotherapy. *Cell* *168*, 707-723.
- 925 Sharma, P., Siddiqui, B. A., Anandhan, S., Yadav, S. S., Subudhi, S. K., Gao, J., Goswami, S., and Allison, J. P.
926 (2021). The Next Decade of Immune Checkpoint Therapy. *Cancer Discov* *11*, 838-857.
- 927 Shen, L., Evel-Kabler, K., Strube, R., and Chen, S. Y. (2004). Silencing of SOCS1 enhances antigen presentation by
928 dendritic cells and antigen-specific anti-tumor immunity. *Nat Biotechnol* *22*, 1546-1553.
- 929 Shi, P., Murphy, M. R., Aparicio, A. O., Kesner, J. S., Fang, Z., Chen, Z., Trehan, A., and Wu, X. (2021). RNA-
930 guided cell targeting with CRISPR/RfxCas13d collateral activity in human cells. *bioRxiv*, 2021.2011.2030.470032.
- 931 Srikrishna, G. (2012). S100A8 and S100A9: new insights into their roles in malignancy. *J Innate Immun* *4*, 31-40.
- 932 Tang, X. E., Tan, S. X., Hoon, S., and Yeo, G. W. (2022). Pre-existing adaptive immunity to the RNA-editing enzyme
933 Cas13d in humans. *Nat Med* *28*, 1372-1376.
- 934 Tang, Z., Kang, B., Li, C., Chen, T., and Zhang, Z. (2019). GEPIA2: an enhanced web server for large-scale
935 expression profiling and interactive analysis. *Nucleic Acids Res* *47*, W556-W560.
- 936 Tormoen, G. W., Crittenden, M. R., and Gough, M. J. (2018). Role of the immunosuppressive microenvironment in
937 immunotherapy. *Adv Radiat Oncol* *3*, 520-526.
- 938 van Spruiel, A. B., Puls, K. L., Sofi, M., Pouniotis, D., Hochrein, H., Orinska, Z., Knobloch, K. P., Plebanski, M.,
939 and Wright, M. D. (2004). A regulatory role for CD37 in T cell proliferation. *J Immunol* *172*, 2953-2961.
- 940 Wang, D., Tai, P. W. L., and Gao, G. (2019a). Adeno-associated virus vector as a platform for gene therapy delivery.
941 *Nat Rev Drug Discov* *18*, 358-378.
- 942 Wang, G., Chow, R. D., Bai, Z., Zhu, L., Errami, Y., Dai, X., Dong, M. B., Ye, L., Zhang, X., Renauer, P. A., *et al.*
943 (2019b). Multiplexed activation of endogenous genes by CRISPRa elicits potent antitumor immunity. *Nature*
944 *Immunology* *20*, 1494-1505.
- 945 Wang, X., Tokheim, C., Gu, S. S., Wang, B., Tang, Q., Li, Y., Traugh, N., Zeng, Z., Zhang, Y., Li, Z., *et al.* (2021).
946 In vivo CRISPR screens identify the E3 ligase Cop1 as a modulator of macrophage infiltration and cancer
947 immunotherapy target. *Cell* *184*, 5357-5374 e5322.
- 948 Wei, J., Lotfy, P., Faizi, K., Wang, E., Slabodkin, H., Kinnaman, E., Chandrasekaran, S., Kitano, H., Durrant, M. G.,
949 Duffy, C. V., *et al.* (2022). Deep learning and CRISPR-Cas13d ortholog discovery for optimized RNA targeting.
950 *bioRxiv*, 2021.2009.2014.460134.
- 951 Wei, S. C., Duffy, C. R., and Allison, J. P. (2018). Fundamental Mechanisms of Immune Checkpoint Blockade
952 Therapy. *Cancer Discov* *8*, 1069-1086.
- 953 Wessels, H. H., Mendez-Mancilla, A., Guo, X., Legut, M., Daniloski, Z., and Sanjana, N. E. (2020). Massively
954 parallel Cas13 screens reveal principles for guide RNA design. *Nat Biotechnol* *38*, 722-727.
- 955 Wolchok, J. D., Kluger, H., Callahan, M. K., Postow, M. A., Rizvi, N. A., Lesokhin, A. M., Segal, N. H., Ariyan, C.
956 E., Gordon, R. A., Reed, K., *et al.* (2013). Nivolumab plus ipilimumab in advanced melanoma. *N Engl J Med* *369*,
957 122-133.
- 958 Yan, W. X., Chong, S., Zhang, H., Makarova, K. S., Koonin, E. V., Cheng, D. R., and Scott, D. A. (2018). Cas13d
959 Is a Compact RNA-Targeting Type VI CRISPR Effector Positively Modulated by a WYL-Domain-Containing
960 Accessory Protein. *Mol Cell* *70*, 327-339 e325.

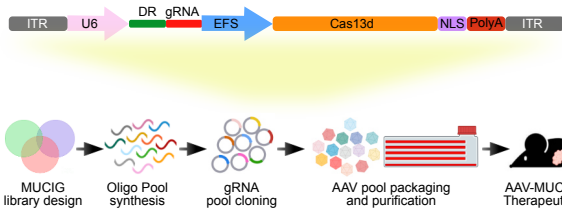
MUCIG Therapy

961

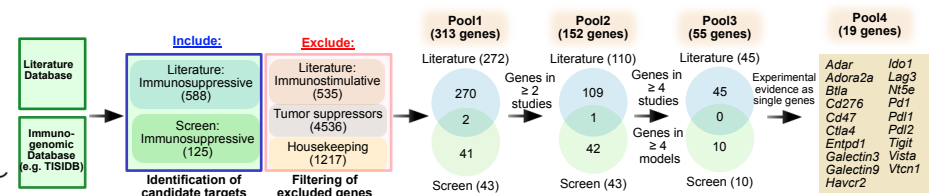
Figure 1

A

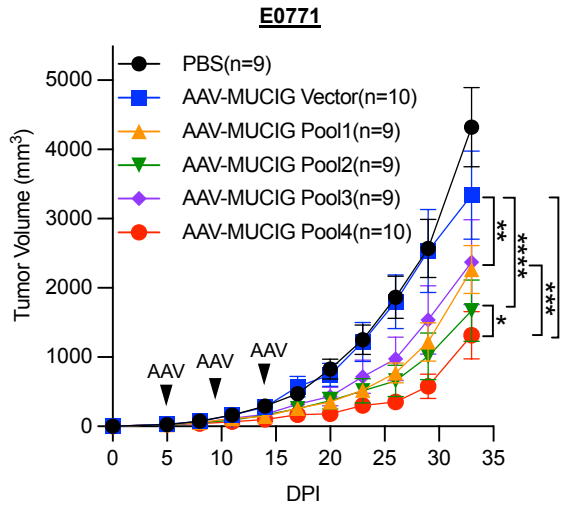
AAV-MUCIG Vector



B



C



D

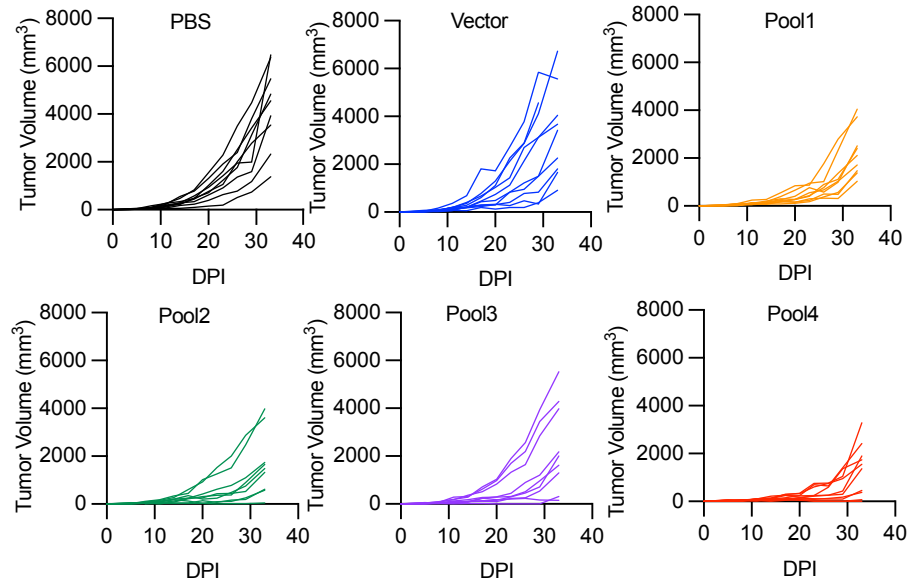
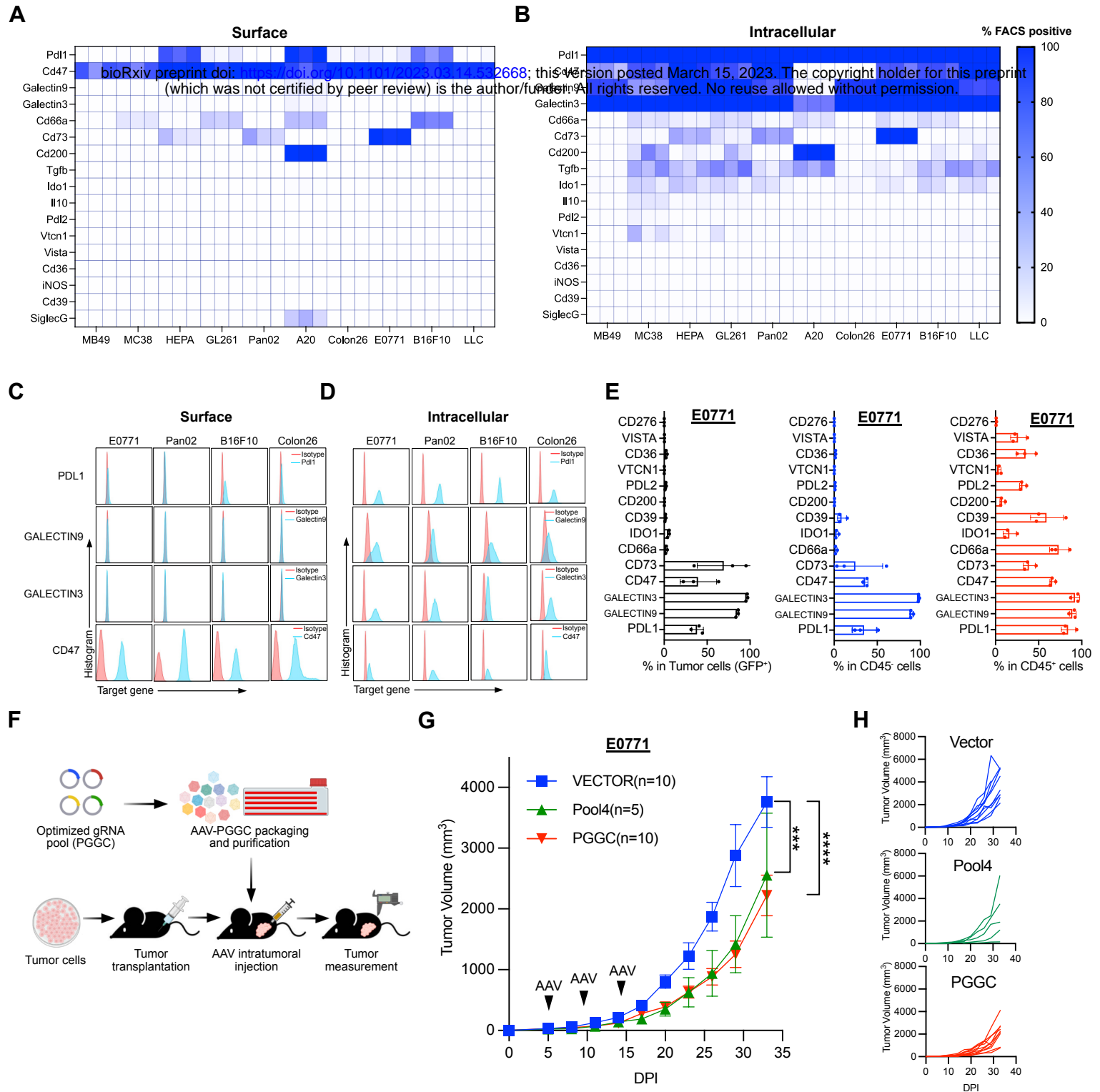
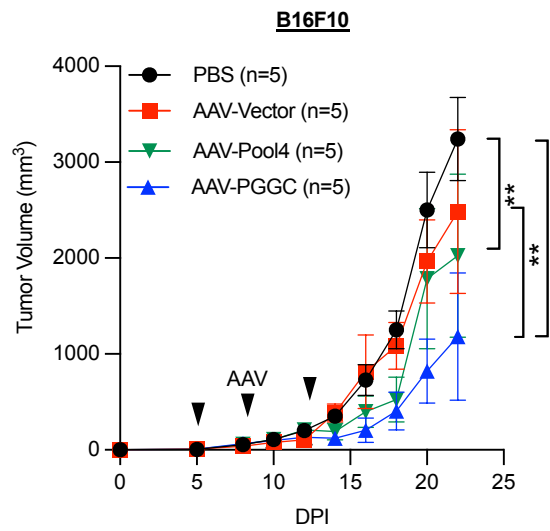
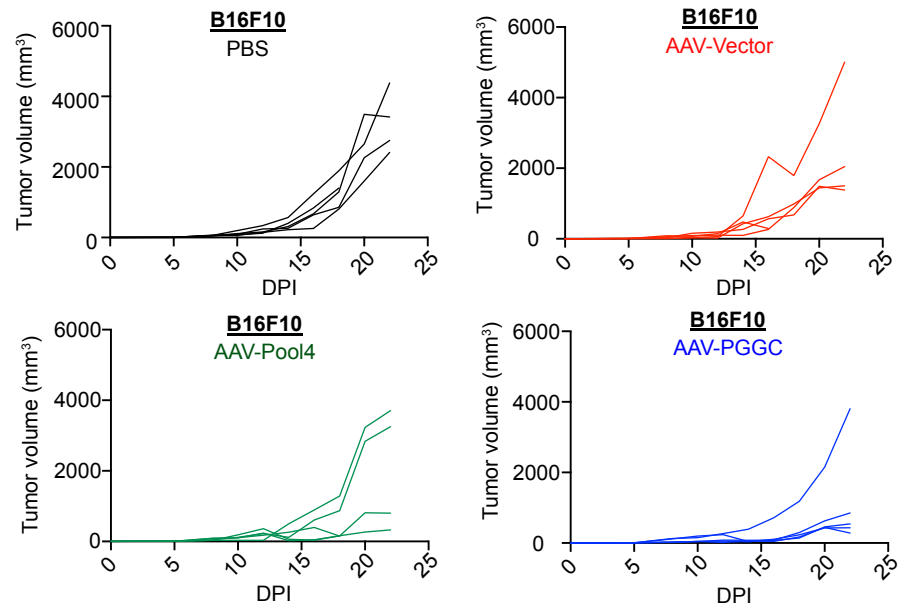


Figure 2

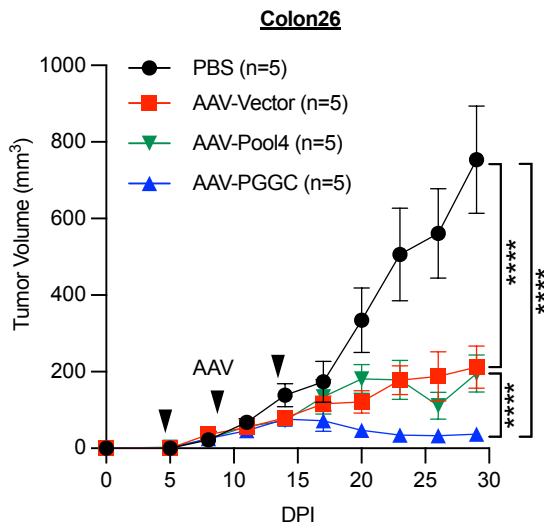
A



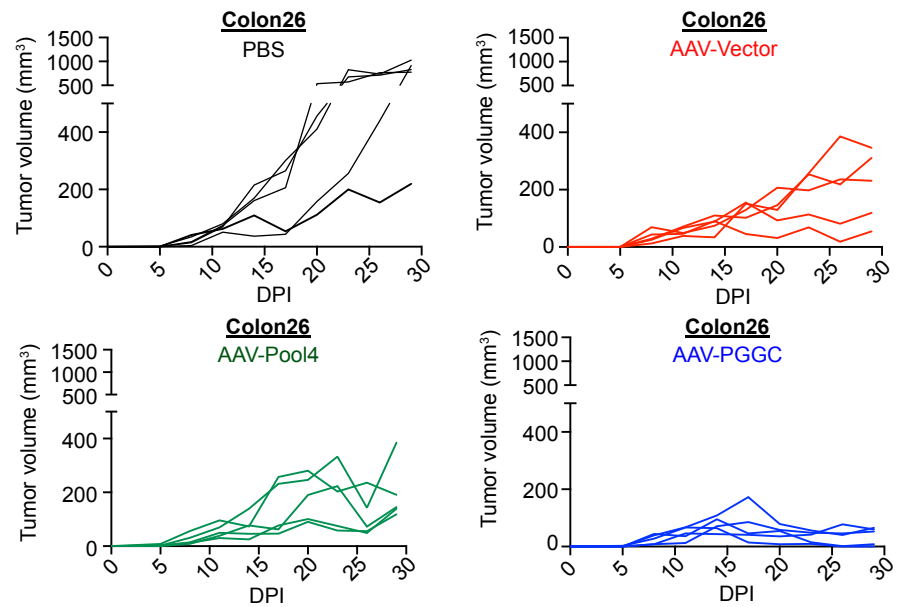
B



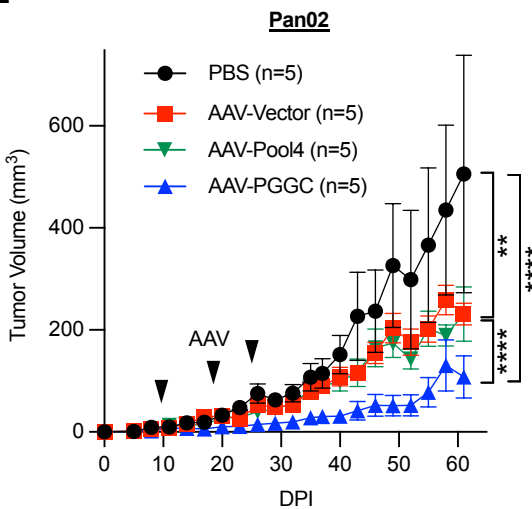
C



D



E



F

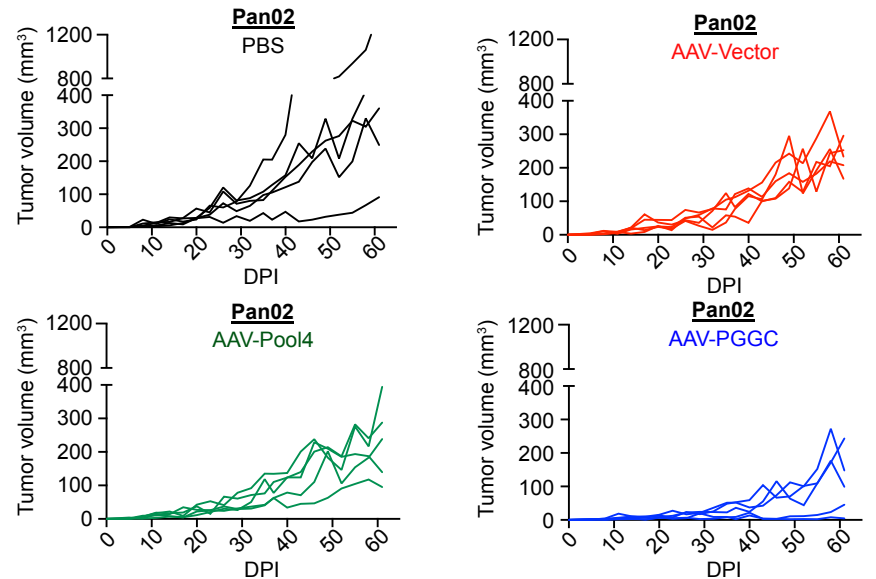
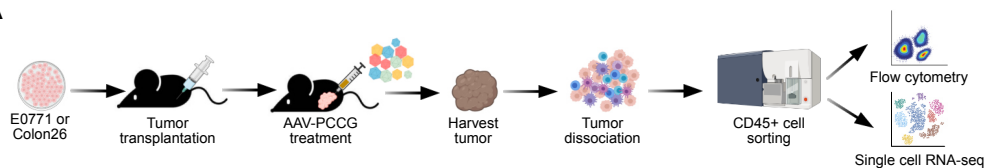
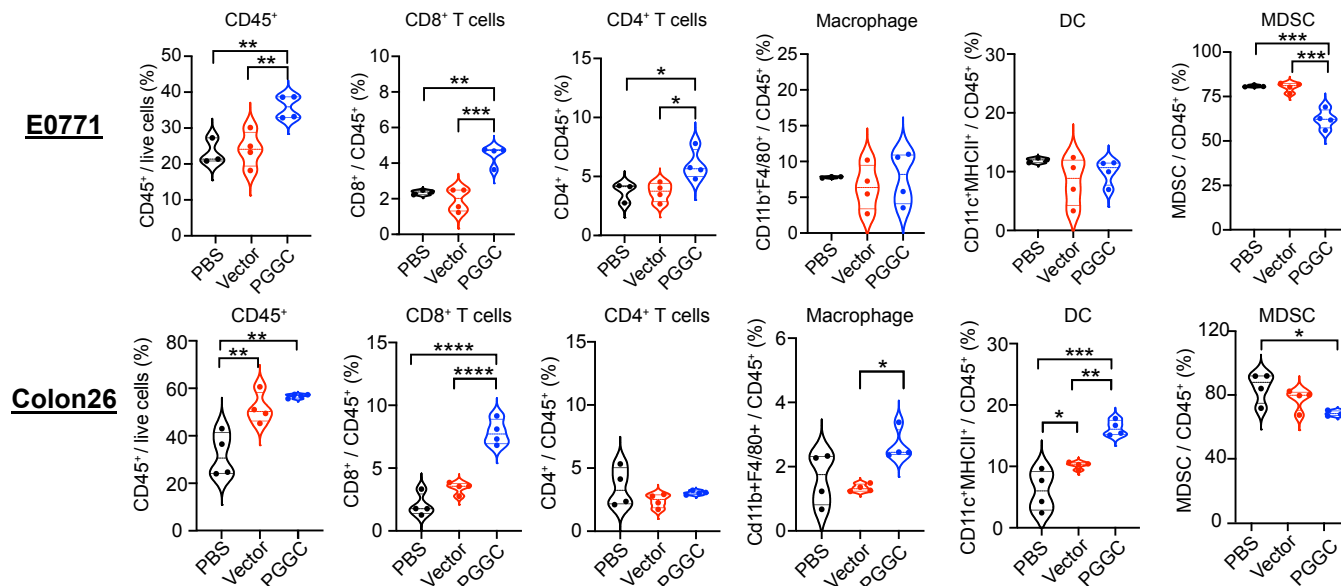


Figure 4

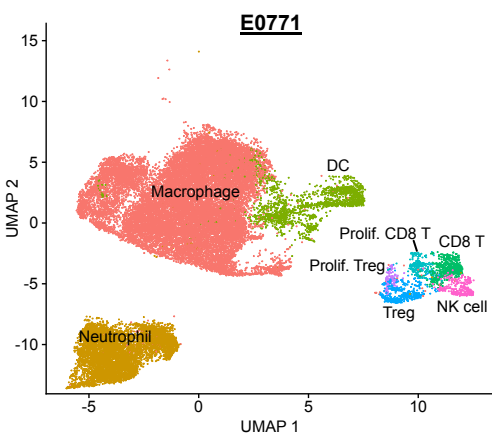
A



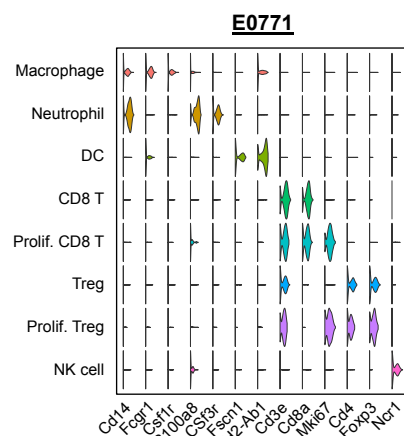
B



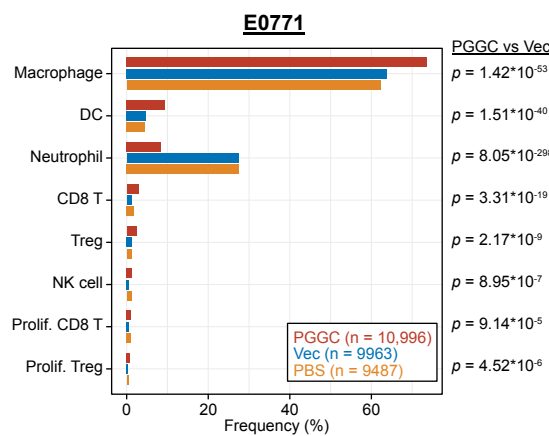
C



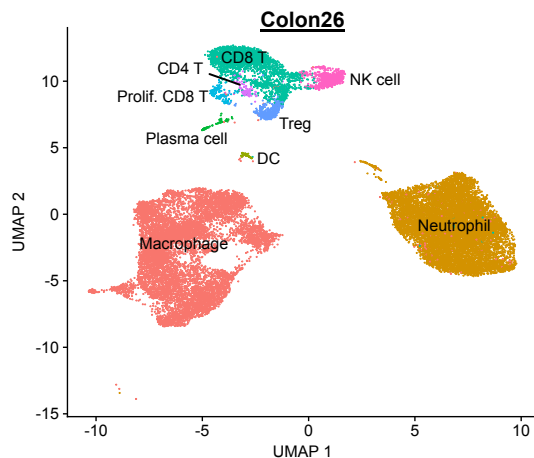
D



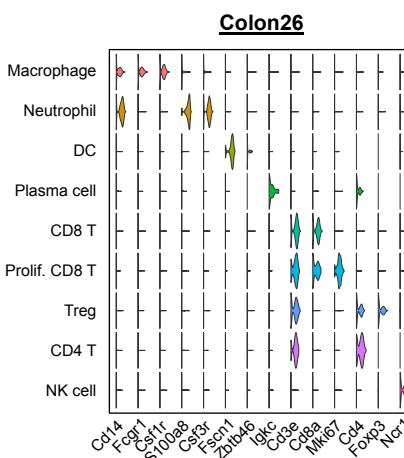
E



F



G



H

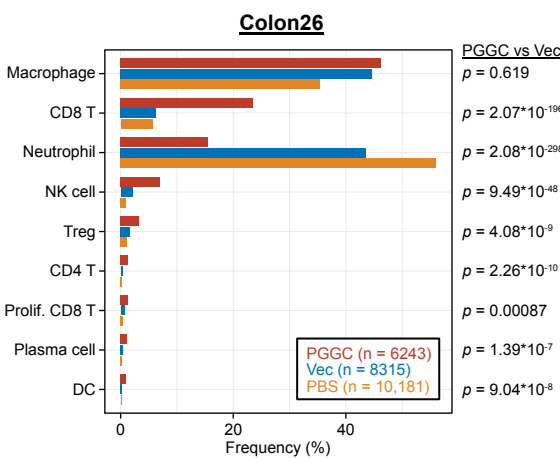
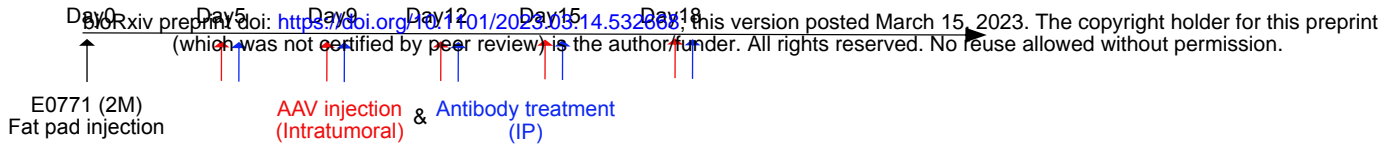
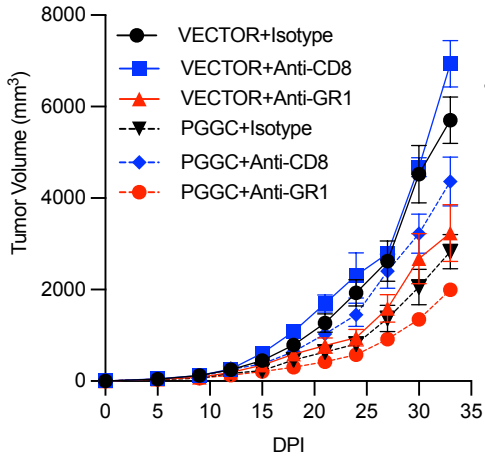


Figure 5

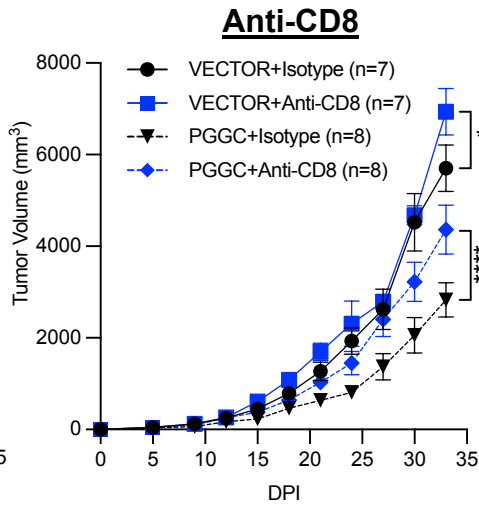
A



B



C



D

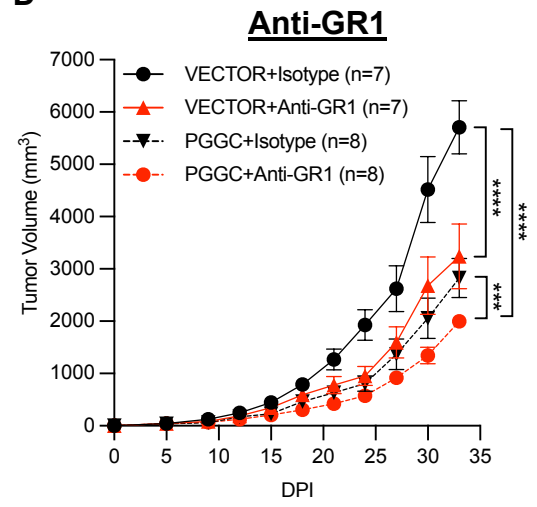


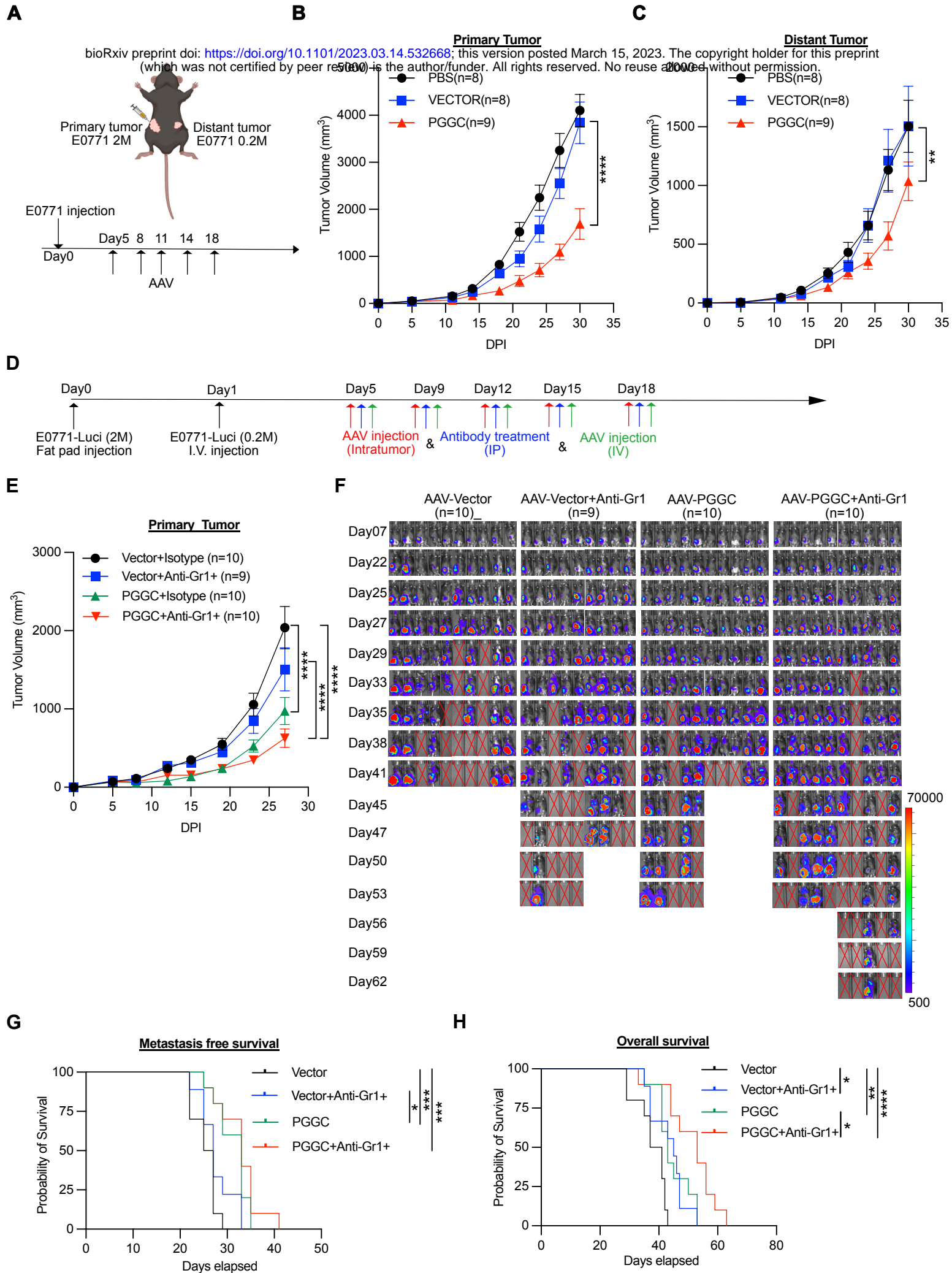
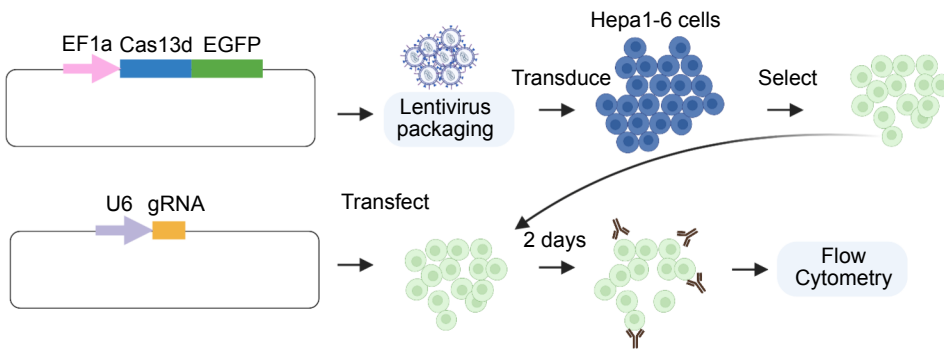
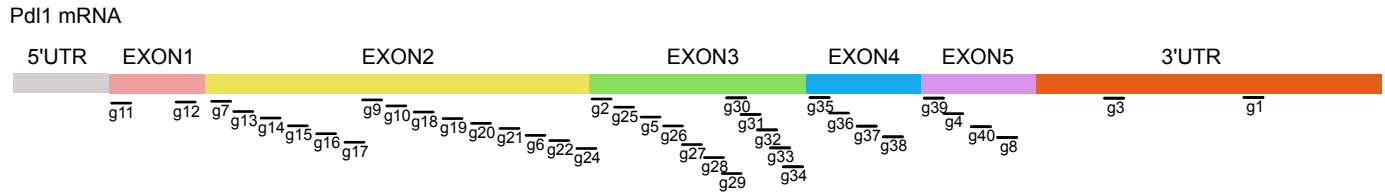
Figure 6

Figure S1

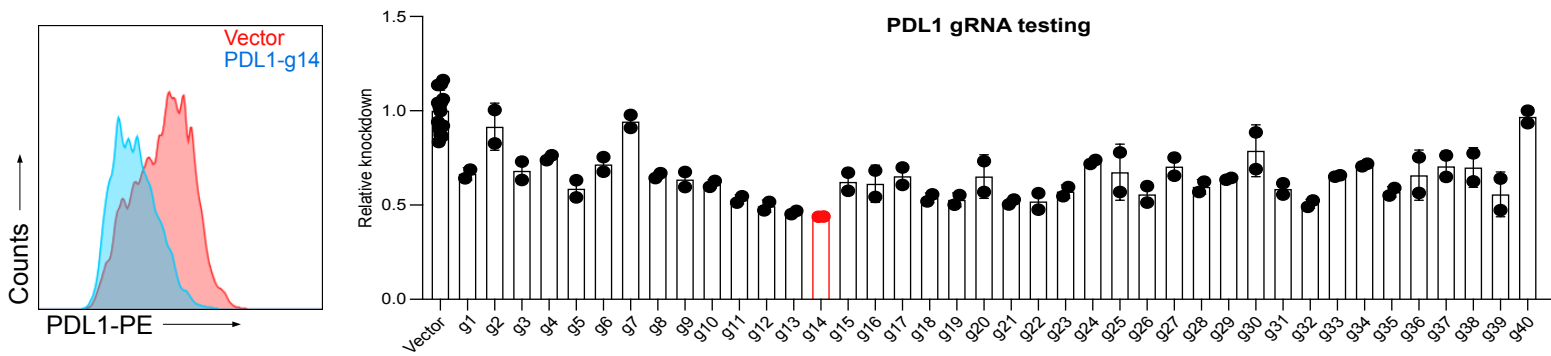
A



B



C



D

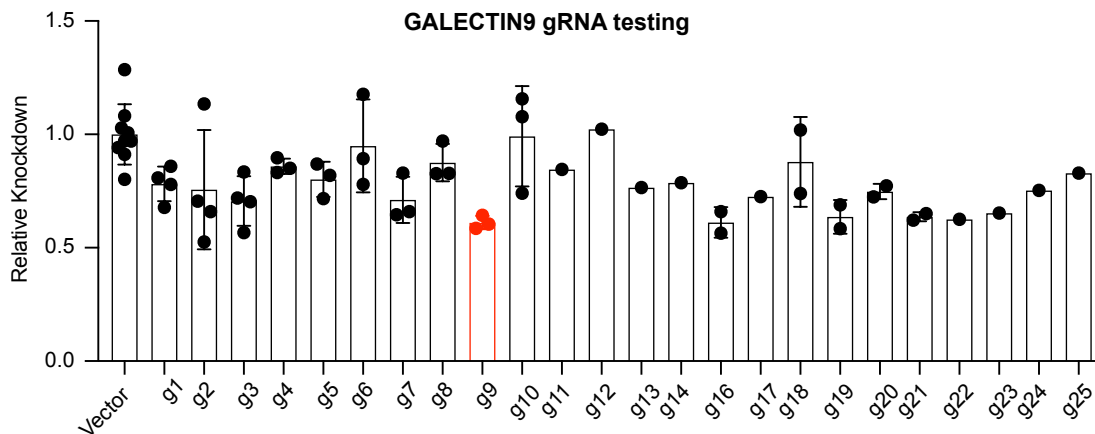
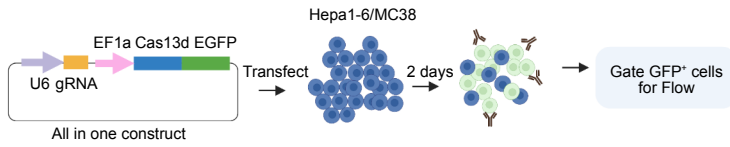
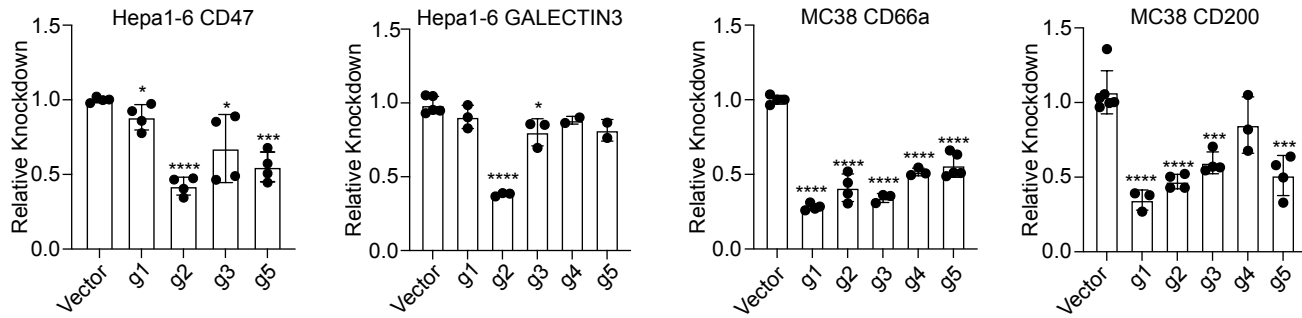


Figure S2

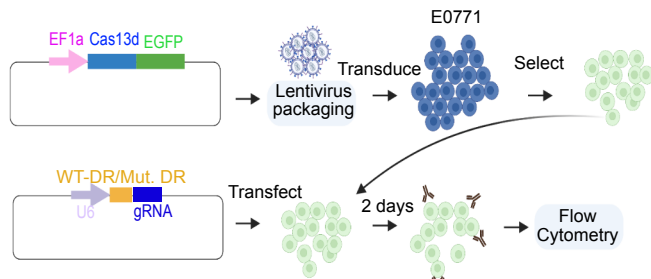
A



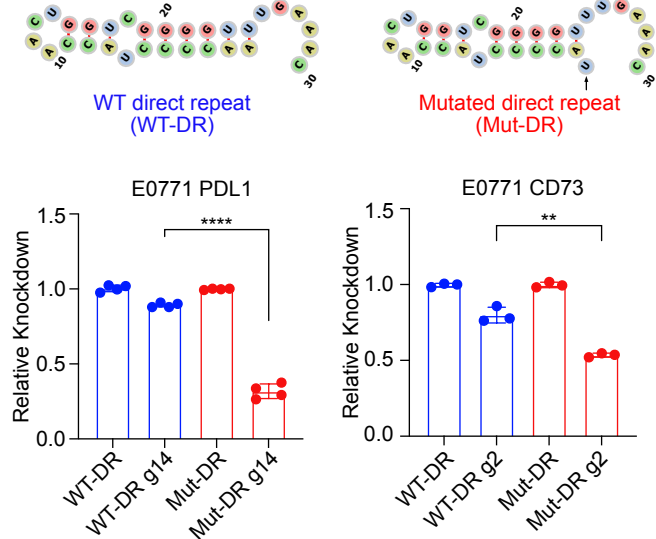
B



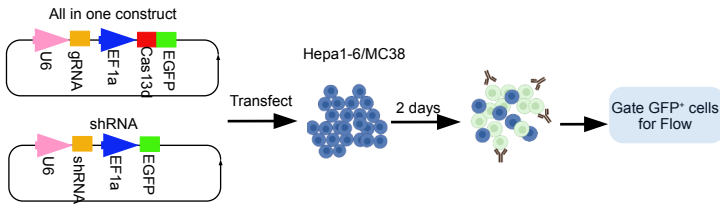
C



D



E



F

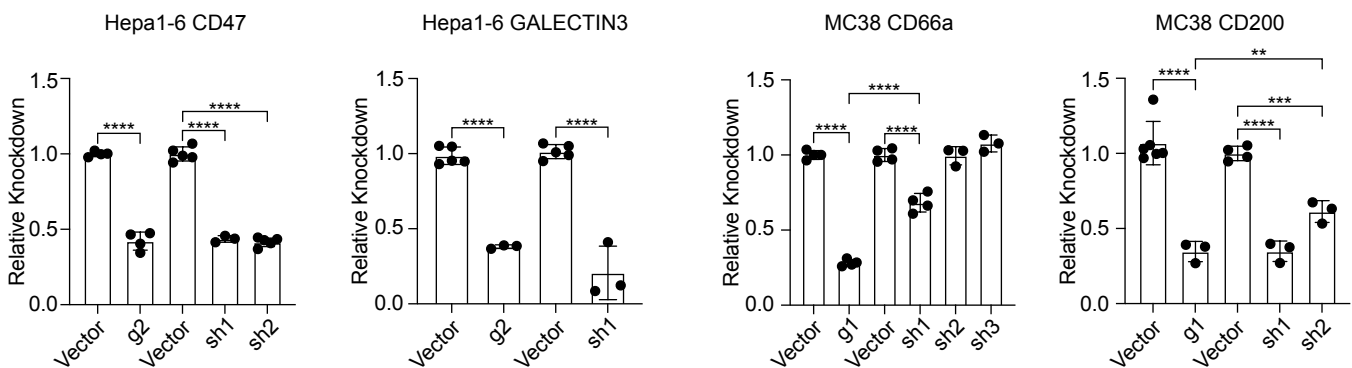
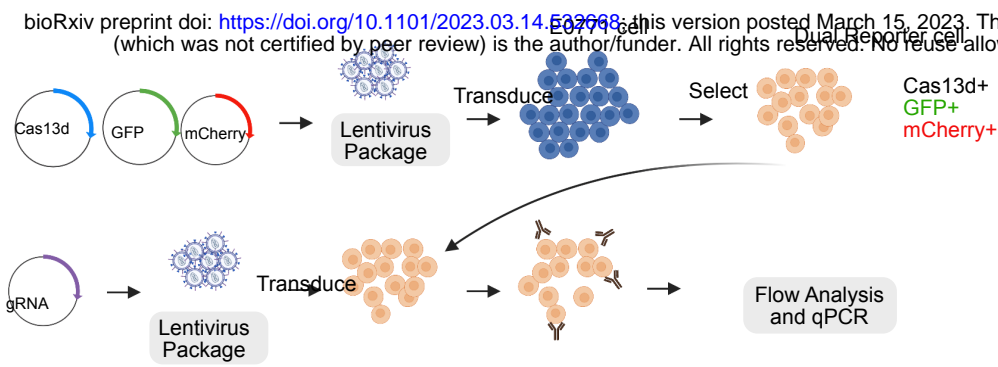


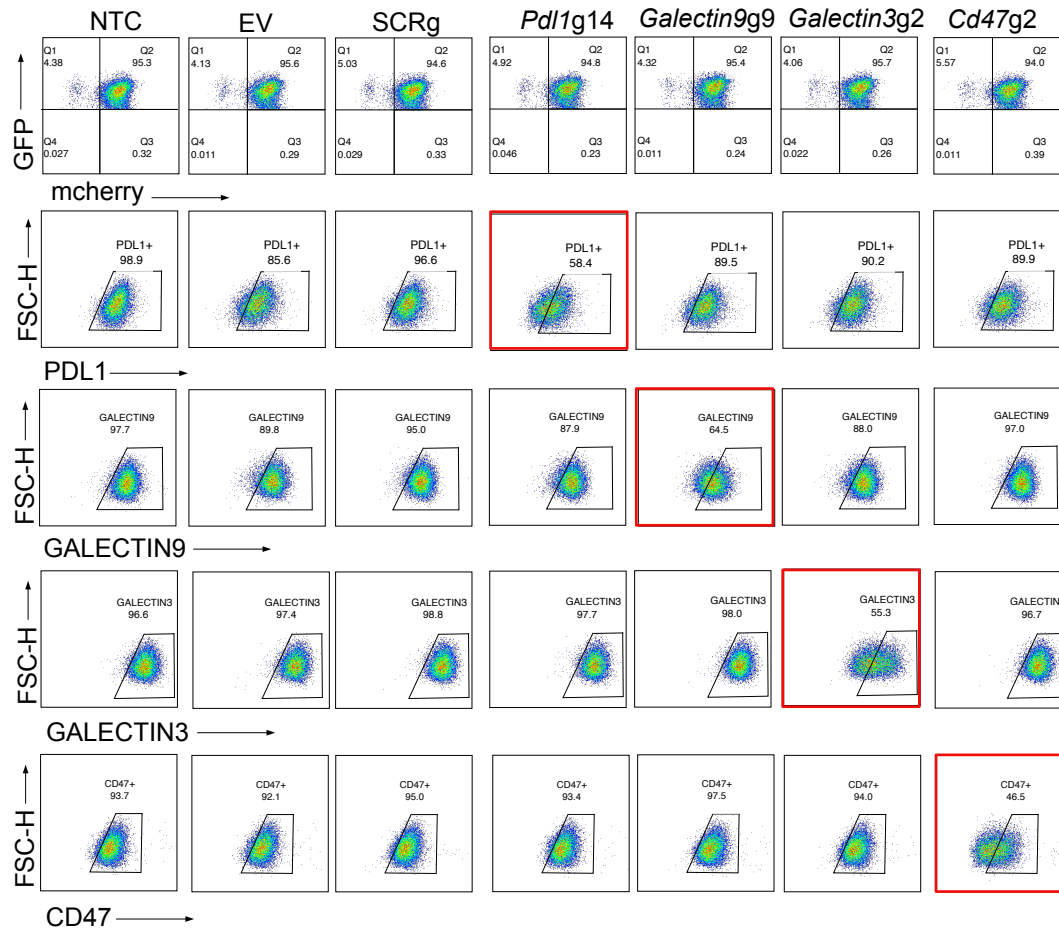
Figure S3

A

bioRxiv preprint doi: <https://doi.org/10.1101/2023.03.14.532968>; this version posted March 15, 2023. The copyright holder for this preprint (which was not certified by peer review) is the author/funder. All rights reserved. No reuse allowed without permission.



B



C

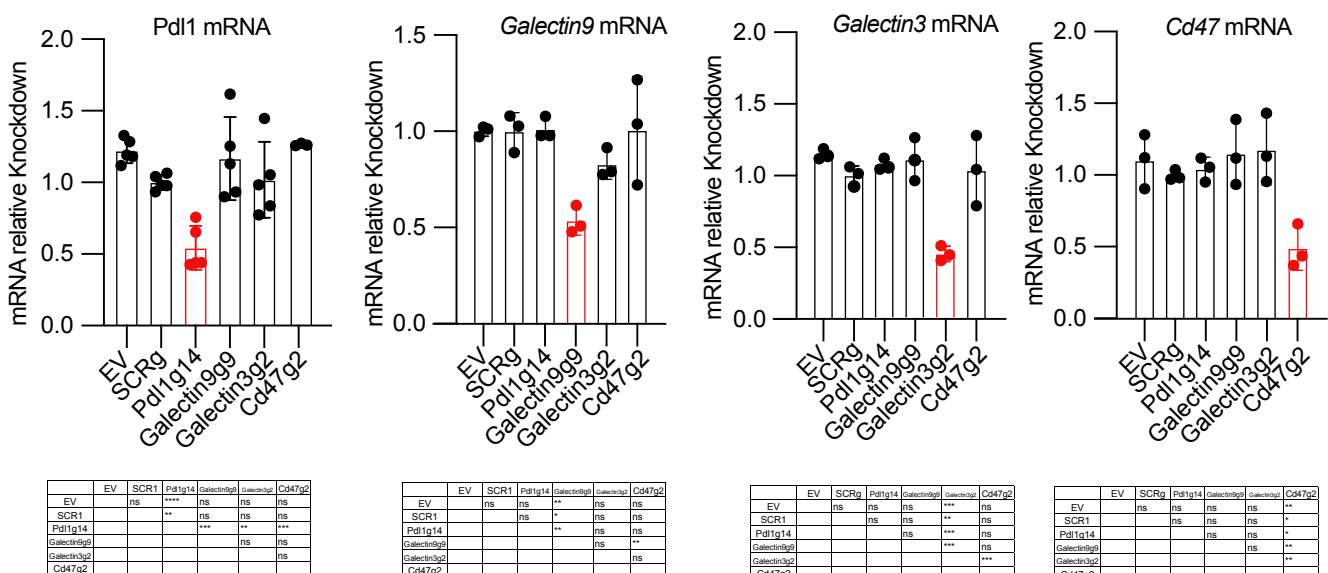


Figure S4

bioRxiv preprint doi: <https://doi.org/10.1101/2023.03.14.532668>; this version posted March 15, 2023. The copyright holder for this preprint (which was not certified by peer review) is the author/funder. All rights reserved. No reuse allowed without permission.

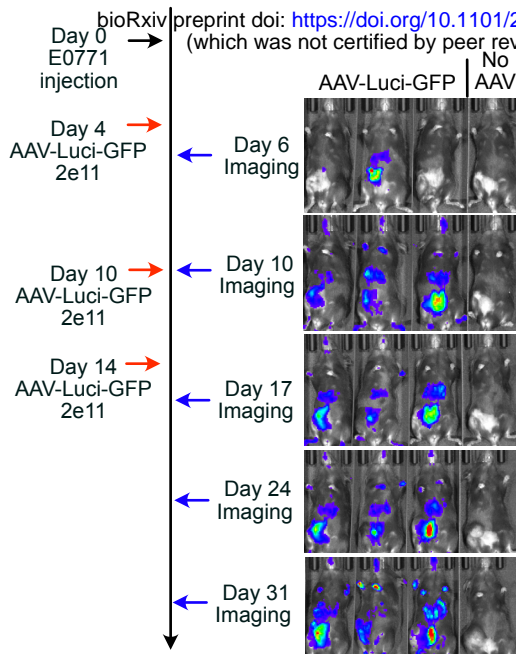
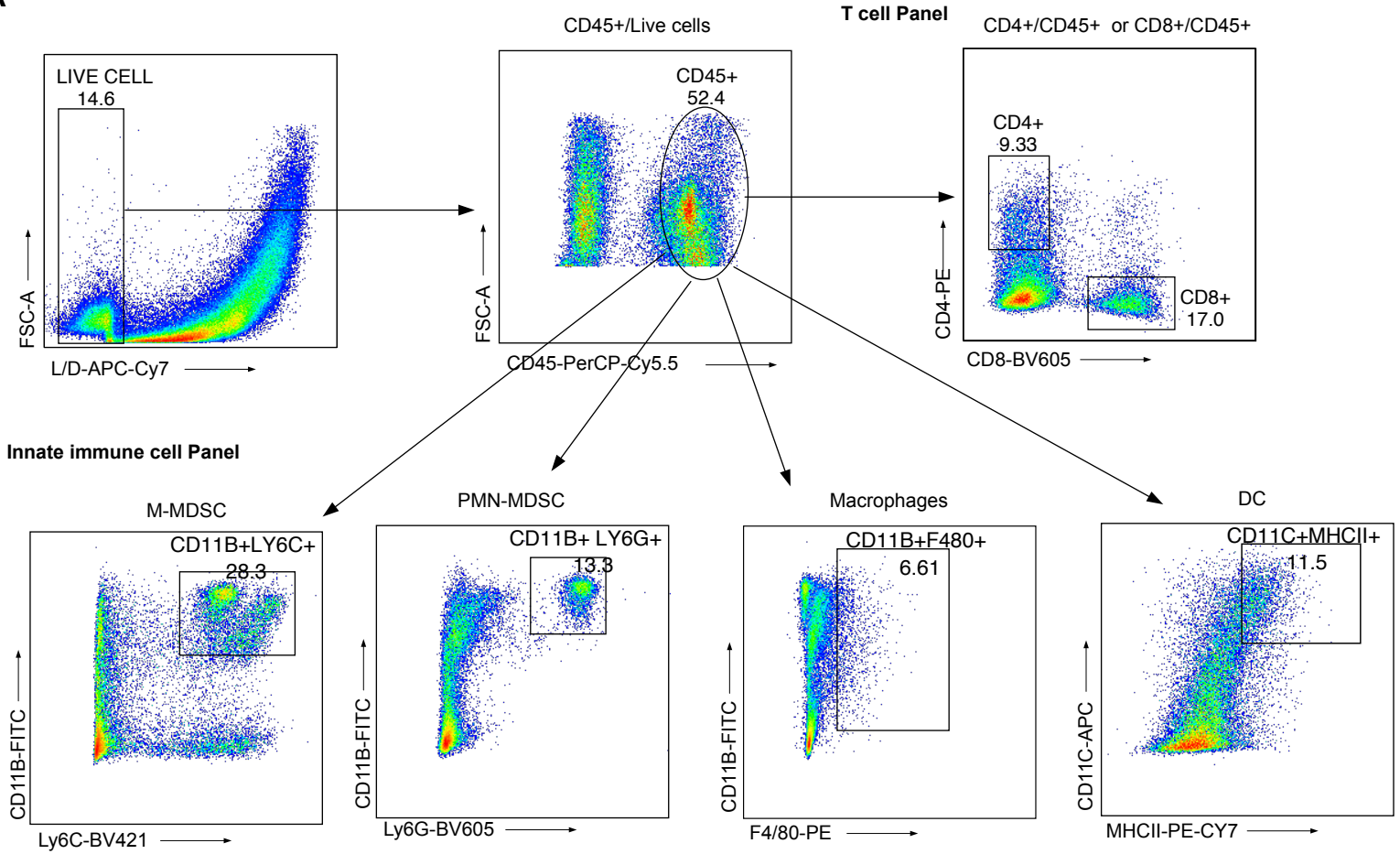
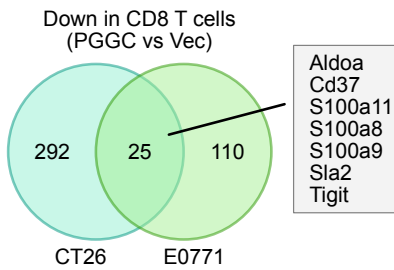


Figure S5

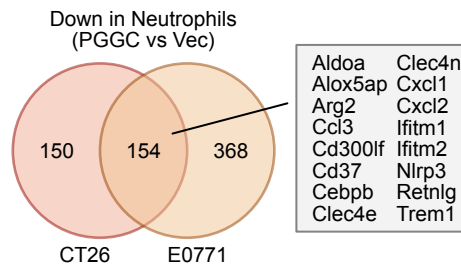
A



B



C



D

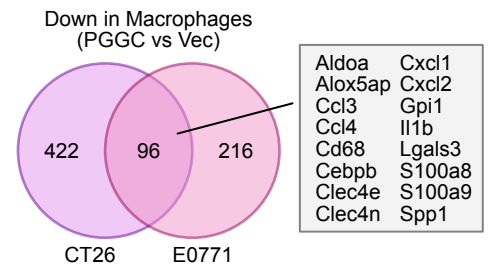
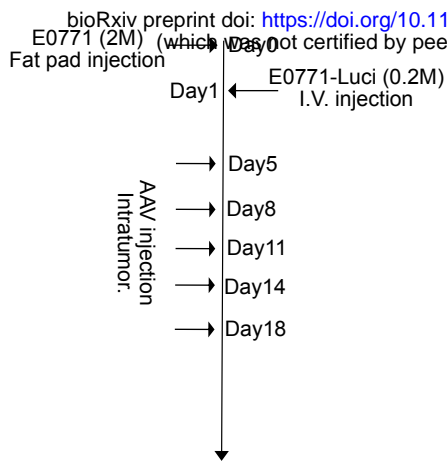
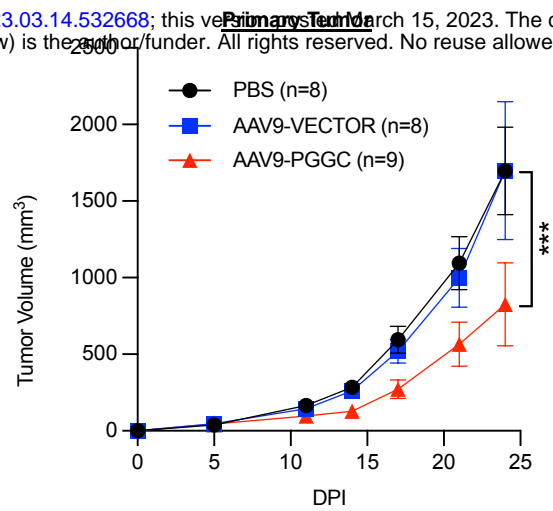
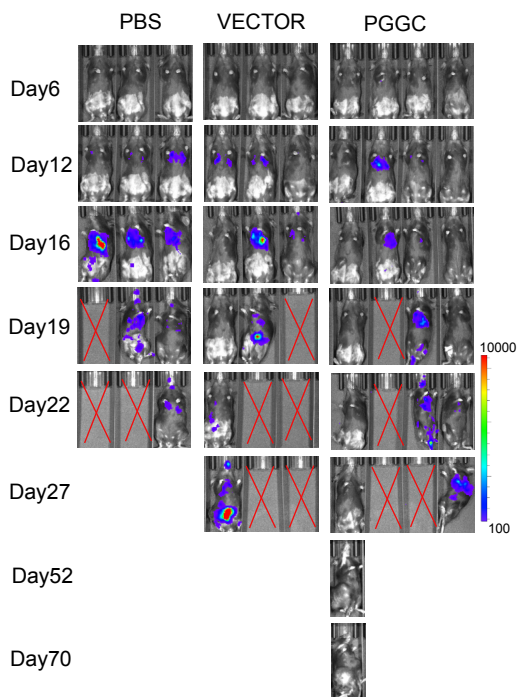
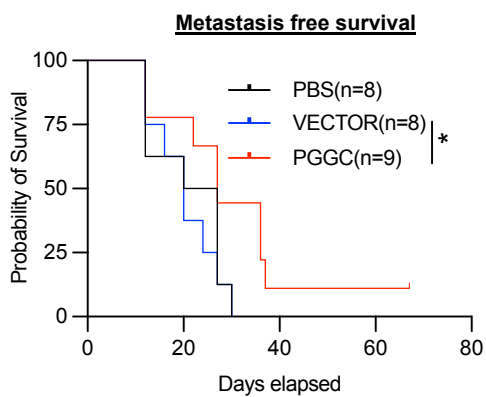


Figure S6**A****B****C****D****E**